行政院所屬各機關因公出國人員出國報告書

(出國類別： 實習)

美國華盛頓大學接受 microPET 核醫藥物臨床前試驗實習

服務機關：行政院原子能委員會核能研究所

出 國 人　職　　稱：薦任助理研究員

姓　　名：張志賢

出國地區：美國

出國期間：91 年 10 月 01 日至 91 年 12 月 31 日

報告日期： 92 年 2 月 20 日

摘　　要

本次赴美國密蘇里州華盛頓大學馬林可研究所(Mallinckrodt Institute of Radiology, MIR)進行 microPET 核醫藥物臨床前試驗實習，此次實際參與實際參與 microPET 之實驗，F-18-Fluorothymidine (FLT) 之細胞吸收(uptake)實驗及參與 F-18-Fluoroacetate (FAC) 之細胞代謝(metabolism)實驗；學習影像分析並建立與相關研究人員之合作關係，有助於核研所與國家衛生院共同購買之 microPET 運轉，並有助於核研所放射藥理實驗室臨床前動物實驗室之建立，其相關經驗亦可做為核研所物理組後續發展動物用正子剖層造影儀(Animal PET)技術之參考。

目　　錄

附表圖目錄

一、目的

本次赴美公差，主要目的有四：

(一) 至密蘇里州華盛頓大學醫學院馬林可研究所(Mallinckrodt Institute of Radiology, MIR)接受microPET動力學訓練，了解馬林可研究所(MIR)的microPET運作模式與目前運轉狀況，有助於核研所放射藥理實驗室運轉及動物實驗模式之建立。

(二) 實際參與microPET之實驗以了解應用microPET進行實驗之規劃實習期間主要與來自日本的學者進行攝護腺癌之動物模式研究並參與該單位之實驗討論。

(三) 參與 F-18-Fluorothymidine (FLT) 之細胞吸收(uptake)實驗。

(四) 參與 F-18-Fluoroacetate (FAC) 之細胞代謝(metabolism)實驗。

本次實習之經驗，了解microPET儀器運轉所須之相關技術執行細節，將對核研所利用此項microPET儀器，無論在實驗技術或分工合作方面有相當助益。

二、過程

(一)本次公差行程如下:

時間	星期	工作內容
10/01-02	二、三	往程,台北至聖路易市(St.Louis,MO)
10/03	四	辦理報到手續 Welch、Anderson 與 Oyama 教授會談
10/04	五	1.與 Oyama 博士討論 10 至 12 月實驗計畫 2.與 kim 博士討論 microPET 影像之分析 3.參加 Daniel Schuster 教授之" Pulmonary gene expression lmaging" micropET 應用研究演講
10/07	一	1 與 Tai 博士討論 microPET 之 Quantification calibration 2. 與 Lee 博士進行 Cu-64 microPET 造影實驗
10/08	二	1. 與 Oyama 博士進行 prostate cancer 實驗
10/09	三	1. 辦理馬林可研究所識別證 2. 與 Jim 博士討論 autoimmune disease micro PET 造影實驗
10/10	四	1. 參加正子輻防執照測驗(PET Radiation Safety Test) 獲得證書 2. 進行 AsiPro 影像分析
10/11	五	1. 參加輻防執照測驗(Radiation Safety Test)獲得證書、配章、指環 2. 進行 AsiPro 影像分析
10/14	一	進行 prostate cancer 細胞實驗
10/15	二	與 John, Lori, Lynne 進行 FDG microPET 造影實驗
10/16	三	與 John 討論 animal holder 相關資料
10/17	四	進行 prostate cancer 細胞實驗

10/18	五	進行 prostate cancer 細胞實驗 2.進行 11C -raclopride 小鼠 microPET 造影實驗
10/21	一	1. 參加 group meeting 討論 microPET 影像實驗 2. 討論 octreotide 之大白鼠動物實驗模式之建立 3. 討論 Analyze 4.0 軟體分析之作業，取得動物影像分析
10/22	二	1. 利用 Analyze 4.0 軟體進行動物影像分析，並整理其相關分析方法 2. 整理完畢寄出 animal holder 尺寸資料(I)
10/23	三	1. 利用 Analyze 4.0 軟體進行 autoimmune disease microPET 動物影像分析，並整理其相關分析方法 2. 整理完畢寄出 animal holder 尺寸資料(II)
10/24	四	學習數據分析
10/25	五	學習數據分析
10/28	一	1. 學習數據分析 2. 查閱論文資料
10/29	二	1. 討論以 microPET 進行藥物動力學之問題 2. 查閱藥物動力學論文資料 3. 與 Oyama 博士討論 FLT 及 FDG 體外細胞吸收(uptake)實驗
10/30	三	1. 與 Oyama 博士進行 FLT 及 FDG 體外細胞吸收(uptake)實驗 2. 討論靜態(static)與動態(dynamic)影像分析
10/31	四	與 Oyama 博士進行 FLT 及 FDG 體外細胞吸收(uptake)實驗

11/01	五	1. group meeting 2. microPET data analysis 3. 討論 TUNEL assay 實驗 4. 進行 DOTA-Antibody 結合實驗
11/04	一	1. 進行 DOTA-Antibody 結合實驗 2. 與 WP 及 Jim 討論 microPET 實驗
11/05	二	1. 64Cu-anti-CD4mAb 之藥動實驗 2. 64Cu-anti-CD4mAb 之生物分佈實驗
11/06	三	1. 64Cu-anti-CD4mAb 之生物分佈實驗 2. 64Cu-anti-CD4mAb 之 microPET 實驗
11/07	四	1. microPET FLT 小鼠實驗 2. 學習動態控制功能(motion control)
11/08	五	1. microPET FDG 小鼠實驗 2. 實習檔案整理並備份 3. 學習動態影像(Dynamic image)重建(Reconstruction)
11/11	一	自體免疫疾病(autoimmune disease) microPET 小鼠 dynamic ROI 數據分析
11/12	二	進行 FDG 及 FLT microPET ROI analysis
11/13	三	閱讀 reference
11/14	四	1. microPET FLT 小鼠實驗 2. FLT 及 FDG 體外細胞吸收(uptake)實驗
11/15	五	1. microPET FDG 小鼠實驗 2. 11C-acetate 體外細胞代謝(metabolism)實驗 3. Group meeting seminar, "Bone metastasis imaging model study"
11/18	一	1. 進行 FDG 及 FLT microPET ROI analysis 2. Group meeting
11/19	二	1. 參加 Dr. Brain 之自體免疫疾病(autoimmune disease) microPET 研究演講

		2. 進行 Dr. Jim microPET ROI analysis
11/20	三	1. Dr. Sun microPET 64Cu- TATE 大鼠實驗與 Dr. Anderson 及 Dr. Sun 討論造影影像結果
11/21	四	1. 進行 Dr. Sun microPET ROI analysis 重點為肝(liver)及腎(kidney)之位置及影像，並與 Dr. Kim 及 Jerrel 討論
11/22	五	1. 進行 F18-fluoroacetate 體外細胞代謝(metabolism)實驗 2. 進行 Dr. Sun microPET ROI analysis
11/25	一	1. 進行 F18-fluoroacetate (FAC)體外細胞吸收(uptake)實驗 2. 進行 Dr. Sun microPET ROI 及 data analysis，並建立表格
11/26	二	讀 reference
11/27	三	1. 讀 reference 2. 進行 F18-fluoroacetate 及 FDG 體外細胞代謝(metabolism)實驗
11/28	四	感恩節國定假日，讀 reference
11/29	五	查閱 FDG 與 microPET 應用之論文
12/02	一	1. Group meeting 2. microPET dynamic ROI 分析
12/03	二	microPET dynamic ROI 及 data analysis，並建立表格
12/04	三	1. FDG and FLT cellular uptake study 2. FDG 及 FLT 小鼠 microPET 影像 ROI 分析
12/05	四	3. FDG and FLT cellular uptake study 4. FDG 及 FLT 小鼠 microPET 影像 ROI 分析
12/06	五	1. FDG 及 FLT 小鼠 microPET 影像 ROI 分析計算

		2. 以 powerpoint 呈現 microPET 影像結果
12/09	一	整理實習之檔案文件
12/10	二	1. 與 Lynnes 討論 "animal husbandry journal"之檔案管理制度，並紀錄其項目 2. 與 Oyama 博士討論 FAC 之實驗結果，並整理
12/11	三	1. 因 micropET 影像分析，與 Lynnes 討論大鼠腎臟與腎上腺之相關位置
12/12	四	與 Oyama 博士討論分析實驗結果，及未來實驗方向
12/13	五	1. 進行 DHT 對細胞株生長影響，一天後細胞計數實驗 2. 計算實驗數據 3. 量各組小鼠 tumor size
12/15	日	1. 進行 DHT 對細胞株生長影響，三天後細胞計數實驗 2. 計算實驗數據
12/16	一	1. 三個月實驗報告演講(II)，題目為 "microPET data collection and data analysis" 2. 與 Jerrel 畫 ROI
12/17	二	1. 進行 DHT 對細胞株生長影響，五天後細胞計數實驗 2. 計算實驗數據 3. 進行 FLT 與 FDG 之 microPET 影像分析
12/18	三	與 Oyama 博士討論分析實驗結果整理報告
12/19	四	與 Oyama 博士討論分析實驗結果整理報告
12/20	五	1 三個月實驗報告演講(II)，題目為

		" Study of FLT and FDG in Androgen Ablation Therapy" 2. 與 Oyama 博士討論
12/23	一	1. 與 John 討論檔案命名，小鼠造影位置關係等 2. 實習檔案整理
12/24	二	1. 影像檔案整理與討論 2. 相關檔案備份
12/25	三	耶誕節國定假日
12/26	四	與 Dr. Kim 學習 data analysis
12/27	五	1. 與 Dr. Welch 及相關教授道別 2. 辦理離開之相關手續及繳交識別證
12/29-31	日-二	回程,聖路易(St.Louis)至台北

三、心得:

(一) 密蘇里州華盛頓大學醫學院介紹:

在 2002 年華盛頓大學醫學院為美國排名第三之醫學院,與 B-J 醫院 (Barnes-Jewish Hospital) 及聖路易市兒童醫院(St.Louis Children Hospital) 座落在一起共同形成醫療研究系統(圖一、圖二),馬林可研究所(Mallinckrodt Institute of Radiology, MIR)是世界上著名的核醫葯物研究與生產中心之一,主要是著重於(Positron Emission Tomography, PET)藥物造影應用,除例行生產放射性核醫葯物供應醫學中心作為臨床使用外,研究人員亦不斷從事新藥之研發,作為診斷與治療,目前使用的核種主要是 C-11、F-18、Cu-64、Cu-61 等,放射科學組(Division of Radiological Sciences)研究人員一半人員負責例行迴旋加速器維護與核醫藥物生產,另一半人員則從事研發工作,除開發研製新藥外,相關的細胞與動物實驗皆由技術純熟的實驗人員進行,而新藥查驗登記前所需要的臨床前實驗、臨床實驗等相關資料撰寫及整理,皆由專人負責,並有核醫葯師協助相關文件審查,作為新藥開發研究人員與美國聯邦食品藥物管理委員會(Food and Drug Administration, FDA)之溝通橋樑,該組研究人員分工清楚,各司其職,本次前往受訓之放射科學

組，與核研所已建立友誼與合作關係，該組組長Welch 教授於 2000 年受邀來核研所參加「同位素與輻射應用研討會」發表專題演講，核研所亦曾有同仁前往實習，張員並於 1999 年前往開會時，就臨床前核醫藥物實驗室請教 Welch 教授該所之經驗，並於 2000 年八月與本所物理組黃世文先生就 microPET 之硬體維護與應用再次前往華盛頓大學做相關討論，並討論張員於十月份前往實習三個月之事宜，獲 Welch 教授同意，辦理邀請函及後續實驗規劃事宜，並於十月至十二月順利前往該校實習三個月；MIR 放射科學組在該組組長領導與各計劃主持人努力配合下，發揮良好的工作效率，這是該所在世界核醫界佔有一席之地的原因。

核能研究所與國家衛生研究院合作計劃購置之 microPET R4 已於 2002 年八月底安裝，MicroPET 主要提供非侵入性(non-invasive)活體(in vivo)功能性影像，藉由正子核種標幟之放射性同位素藥物注射進入動物體，以 microPET 進行及時影像擷取(acquisition)，經由影像重組(reconstruction)與分析(Image analysis)之後，能夠獲得藥物在體內之動態影像(Dynamic visualization)，瞭解藥物的動力學狀態與產生藥效時間的參考資料，再進一步搭配生物體分佈實驗

(Biodistribution)，以確認藥物之分佈情形。microPET 主要是由活體獲得動態藥物資訊，減少動物犧牲數目，由動態實驗數據，得到不同時間藥物濃度後，能進一步計算藥物動力學參數；在新藥開發應用上可進行新藥快速篩選(High-Throughput screen)，直接由動物體之反應與藥效，篩選出有效新藥。華盛頓大學醫學院放射科學組已於 2000 年 12 月安裝與核研所相同之 microPET R4 機型，並累積將近二年之運作經驗，前往該所實習其 microPET 動物造影實驗室(圖三、圖四)規劃、儀器擺設與實驗操作動線之經驗，皆有助於核研所未來 microPET 動物造影實驗之進行。

(二) 張員到達華盛頓大學後，為配合學校之規定，所有操作放射性同位素人員必須通過相關考試獲得證書才能進行實驗，因此本人於十月中旬參加輻防執照測驗(Radiation Safety Test)獲得證書、配章、指環，並參加正子輻防執照測驗(PET Radiation Safety Test)獲得證書後才正式參與放射性同位素實驗之操作。

(三) 實習期間參與 microPET 數據擷取與分析: 該所制度是由研究人員填寫影像需求表與數據分析表，統一安排專人進行動物實驗與操作 microPET 造影時間；其使用之軟體有三種，包含 1.

microPET Manager™ 軟體:由 Concorde 公司隨儀器附上，作為電腦系統與 microPET 之連接媒介，以進行影像擷取與重建；其軟體主視窗就實驗研究人員而言，包含 Investigator Configuration，此為擷取協定設定(Acquisition Protocols)，提供實驗設計者設定個人及不同實驗之各協定參數，若研究人員事先已知其造影與所需之影像數據呈現時間點，可以將影像重建需求資料輸入電腦，當影像擷取完後電腦便能自動進行影像重建。主要參數設定:(1)Acquisition Mode：選取掃描型式，(2)Acquisition Time：設定掃描時間，(3)同位素(Isotope)藥物選取，正子藥物經由動物體內發射後，訊號被 microPET 接收，經數據擷取後儲存為 List Mode。原始數據(List Mode)最後經影像重建(Reconstruction)後，儲存為影像重建數據(Image File)。2. ASIPro (Acquisition Sinogram and Image Processing)軟體，由 Concorde 公司隨儀器附上，作為影像呈現之功能，當點選 File 可出現 Sinogram 視窗及 Image 視窗，在 Image 視窗下點選 Display/Orthoviewer 出現顯示 Transverse、Coronal、Sagittal 三個影像，點選 Display/Tools/ROI 出現，若系統已完成 Normalization、Quantification Correction，在此視窗下圈選 ROI 可完成定量分析。除了建立(Set-up)

及診斷硬體系統初始狀態外，主要提供影像重建之影像顯示及利用 ROI (Region of Interesting)工具做 2D 與 3D 定量分析，作數據之統計分析。由於華聖頓大學延續其早期 2D 數據分析方式此軟體每一片影像切面(plane)之數據需單獨存檔並不方便故他們使用 Analyze 4.0 軟體。3. Analyze 4.0 軟體：由醫院研發團隊所發展，他們能夠將所圈選 2D ROI 得到的數據及影像儲存於同一個檔案中，保存每一切面（plane）的原始數據，方便後續的資料檢閱與計算；目前該所使用 Asipro 作為影像擷取及重建，決定腫瘤器官所需分析的切面數目，然後再由 Analyze 4.0 軟體進行分析計算。另外在進行 ROI 圈選時，Asipro 只能進行 Transverxial 切面之圈選，而 Analyze 4.0 可進行 Transverxial、coronal、sarggital 切面之圈選。因此當影像在 Transverxial 切面受干擾時，可進一步使用 coronal 或 sarggital 切面進行 ROI 之圈選及計算，功能比 Asipro 多，因此目前例行性數據運用上述軟體進行分析。

(四) 張員於實習期間參與實驗之一為 F-18 -Fluorothymidine (FLT)應用於攝護腺癌之體外(In vitro)細胞實驗與體內(In vivo)動物實驗模式研究，目前針對攝護腺癌之治療(Androgen Ablation Therapy)在臨床上有數種方法:

1. 使用 LH-RH 促進劑 (Luteinizing Hormone-Releasing Hormone agonist)：此法能停止雄性激素(Androgen)之分泌。
2. 去勢(castration)：這是治療攝護腺有效方法之一，但是一般病人較不願做此法治療。
3. 雌性激素(Estrogen)：使用 DES(diethylstilbestrol)治療，以抑制攝護腺癌之生長。
4. 抗雄性激素藥物(Anti-androgen drugs)：如flutamide，以阻斷雄性激素受體(Androgen Receptor)之作用。

對於疾病之早期診斷與治療目前仍是醫學研究之重點，因此研發新的造影以達到早期診斷攝護腺癌之目的；此計畫由來自日本的 Oyama (Nobuyuki Oyama)博士所主導，他為華盛頓大學之客座助教授，本身亦為泌尿科醫師，其研究主題主要為攝護腺癌之核醫正子造影劑開發，他之前之研究亦已證明 FDG 在攝護腺癌之早期診斷上並不適合，因此在 Welch 所長支持下與 Ponde 博士共同進行此項研究，Ponde 博士負責合成 FLT，而 Oyama 博士負責其 FLT 之生物相關實驗，目前此一研究已有初步結果，並已發表於 2002 年美國核醫年會。

Oyama 博士之前的實驗是應用 CWR22 雄性激素依賴型腫瘤細胞株(androgen dependent cell

line)種植於裸鼠，腫瘤細胞於小鼠身上生長二週後，進行 microPET 造影，作為實驗前之腫瘤標準大小實驗，之後分為三組，第一組為治療實驗組:小鼠進行去勢，當移去睪丸之後，腫瘤會停止生長；第二組亦為治療實驗組，小鼠施打 DES (diethylstilbestrol)雌性賀爾蒙類似物(Estrogen Analog)，此要會停止腫瘤生長；第三組為對照組，不作任何處理，使腫瘤繼續生長，之後所有小鼠每一週進行造影，並測量腫瘤大小及進行生物體分佈實驗(Biodistribution)，以了解對攝護腺癌之造影效果；結果利用 FLT 及 microPET 分析發現，在小鼠動物模式中 FLT 的確能夠被攝護腺癌細胞攝取，經由去勢與雌性賀爾蒙類似物治療之小鼠對 FLT 之攝取比對照組低。

FDG 造影原理是將葡萄糖第二個碳位 OH 基在合成過程中以氟(F-18)取代，造成腫瘤因醣解作用(Glycolysis)較發達而攝取較多 FDG，FDG 被磷酸酵素磷酸化後蓄積於腫瘤細胞中，以達到腫瘤造影效果；但在攝護腺癌細胞因生長較慢，FDG 不適用作為攝護腺癌造影劑。FLT 是 Thymidine 類似物，當細胞染色體複製時就會利用 FLT，當它被正複製之腫瘤細胞磷酸酵素磷酸化後，它便蓄積於腫瘤細胞中以達到腫瘤造影效果，因此理論上 FLT 較為敏感，其造影效果在攝護腺癌應比

FDG 優良。因此 10 月至 12 月在華盛頓大學實習期間延續之前研究，在動物模式方面，使用去勢組及雌性激素治療組作為裸鼠動物模式，比較 FDG 及 FLT 對早期診斷攝護腺癌之效果，同時利用細胞實驗研究 FLT 之攝取是否和癌症細胞增值活性(Proliferative Activity)成正比。

10 月至 12 月之研究分為體外(In vitro)細胞實驗與體內(In vivo)動物實驗；體外(In vitro)細胞實驗方面，使用 PC-3 攝護腺癌雄性激素非依賴型細胞株(Androgen independent cell line)及 LNCap 雄性激素依賴型細胞株(androgen dependent cell line)。首先若在實驗前，PC-3 雄性激素非依賴型細胞株使用血清培養基及無血清培養基(serum free medium)培養此細胞 24 小時後，加入 FDG 及 FLT，以分析其細胞增值時，攝取 FDG 及 FLT 之速率。

結果顯示在無血清培養基中，因細胞增值速率非常慢，因此對 FDG 及 FLT 之攝取低，但 FLT 在血清培養基中之增值細胞攝取量高，再與 FDG 之攝取百分比比較，可明顯看出 FLT 比 FDG 優良。實驗結束後，細胞亦使用細胞流數分析儀(Flow cytometry)分析其細胞週期 S 時期之比例，可以進一步了解此一結果，證實在一般血清培養基之細胞其 S 時期比例大於在無血清培養基之細

胞。

若使用 LNCap 雄性激素依賴型細胞株，使用一般血清培養基之細胞為對照組，Charcoal/Dextran 處理之培養基以除去類固醇 steroid (含 testasterone)，使用 LNCap 細胞株停止生長，作為 Androgen Ablation Therapy 之模式，在加入不同濃度之雄性激素 DHT(Dihydrotestosterone)以刺激細胞增值，並加入 FDG 及 FLT，分析兩種藥物對增值細胞攝取之比例，實驗證明在依賴型細胞株使用 Charcoal/Detran 處理之培養基培養後，對 FLT 之攝取大幅降低，在加入不同濃度之 DHT 後，FLT 攝取量增加，在與 FDG 之攝取百分比比較，可明顯看出 FLT 比 FDG 優良。實驗結束後細胞亦使用細胞流數分析儀分析其細胞週期 S 時期之比例，可以知道在一般培養基之細胞其 S 時期比例大於在 Charcoal/Detran 處理之培養基培養之細胞。因此體外細胞實驗模式證明在比較 FDG 與 FLT 對於攝護腺癌之攝取上，FLT 比 FDG 優良。

在動物實驗模式方面，本次實驗使用 LAPC-4 攝護腺癌雄性激素依賴型細胞株，將此細胞株種植小鼠二週後，進行 microPET 造影，作為實驗前之腫瘤標準大小實驗，之後實驗分為二組，第一組為治療實驗組:小鼠進行去勢，當移去睪丸之

後，腫瘤會停止生長；第二組為對照組，不作任何處理，使腫瘤繼續生長，之後小鼠一週後進行造影，再進行 microPET 造影，以比較 FDG 與 FLT 對於攝護腺癌在動物模式之攝取，在進行數據分析後，此一實驗初步看來 FLT 比 FDG 優良，但因張員在華盛頓大學時間有限，後續實驗將會繼續進行。

(五) 張員實習期間亦參與 F-18-Fluoroacetate (FAC) 之細胞代謝(metabolism)實驗，乙酸(acetate)能夠參與細胞之醣解作用，亦參與細胞之脂肪合成(Lipid Synthesis)，在癌細胞之複製過程中由於細胞分裂所需，亦需要進行脂肪合成，以利細胞膜合成所需，因此 FAC 能夠被癌細胞攝取達到造影效果，在 Welch 所長支持下，Oyama 博士與 Ponde 博士共同進行 FAC 應用於攝護腺癌動物模式研究，Ponde 博士負責合成 FAC，而 Oyama 博士負責其 FAC 之生物相關實驗，目前此一研究之動物實驗結果，並已發表於 2002 年美國分子影像年會。他之前的實驗是應用 CWR22 雄性激素依賴型腫瘤細胞株(androgen dependent cell line)種植於裸鼠，腫瘤細胞於小鼠身上生長二週後，進行 microPET 造影，在動物實驗中證明 FAC 能夠被含有 CWR22 腫瘤細胞株之裸鼠所應用，在十月至十二月期間主要是進行 FAC 在 LS174 細胞株

之代謝實驗，將 FAC 加入生長中的細胞後，培養分鐘後將細胞打碎分離脂溶性層(Lipid soluble layer)及水溶性層(water soluble layer)，濃縮後，與標準品分析比較其代謝產物；因時間有限張員結束實習時實驗仍在進行，尚未得到最後結論。

(六) 三個月之實習結束前，於該所報告實習內容與實驗進度，十二月十六日第一次報告，題目為“microPET data collection and data analysis”，由於 MIR 的研究工作跨越很多專業領域，例如藥理、化學、生物細胞、臨床病理、統計分析...。雖然利用 microPET 造影的相關研究很多，但是很多研究人員對 microPET 的運作方式及數據分析仍不甚了解，故此一報告能夠幫助對 microPET 應用有興趣的人員對該所 microPET 的運作及數據分析有進一步了解。十二月二十日第二次報告，題目為“ Study of FLT and FDG in Androgen Ablation Therapy”，藉由此次報告亦讓該所研究人員了解由 Oyama 博士及 Ponde 博士進行之 FLT 及 FDG 之細胞與動物實驗最新之研究資訊。

(七) 實習重點之一亦是學習馬林可研究所檔案管理與運作制度，該所為使實驗順利進行採分工制度，細胞有專人培養，動物實驗有專人進行，因此建立相關需求表格由實驗人員填寫，此一方式使該所之研究工作進行非常迅速。運作制度整理如下：

1. 華盛頓大學醫學院馬林可研究所針對 microPET 之運作成立 microPET/Animal Facility，在 MIR 的運作模式與目前運轉狀況為該單位向 National Cancer Institute 申請計畫，將其 microPET/Animal Facility 成立為 Small Animal Imaging Resource center，以維持 microPET 之基本運作，同時以該單位之研究人員為媒介與外界合作，初期可先做動物造影，再以此初步影像結果撰寫研究計畫，申請經費以利後續實驗經費支持及實驗之進行，華盛頓大學為學術機構，他們重視合作研究及論文發表、專利申請，共享研究成果，而不希望純粹進行對外技術服務。
2. 在 microPET 硬體方面，由 Richart Laforest 博士為負責人，Yuan-Chuan Tai 博士與 Ananya Rnangma 博士等三位負責，MIR 與 Concorde 總公司關係密切，因此 MIR 保有一塊 detector 已備不時之需，Tai 博士為 microPET 最早研發人員之一，他除負責機器之 Normalization 及定量校正 (Quantitation Calibration)外，亦繼續 microPET 之研發。
3. 動物實驗操作小組，由 Terry Sharp 負責，John (John Engelbach)及 Lynne (Lynne Jones)負責動物顯微手術及解剖實驗，Lori (Lori Strong)負責 microPET 之操作，Joongyoung Kim 及 Jerrel

Rutlin 負責 ROI 圈選影像數據分析。MIR 進行小鼠腫瘤 FDG 造影實驗判斷腫瘤大小，並進行新藥治療後之療效評估，他們設計之壓克力模具，可使兩隻小鼠並排，同時進行造影研究，此次亦了解實驗室之擺設，氣體麻醉機，顯微手術設備等等，使實驗室能夠在最適宜的環境進行實驗。

4. 為維持儀器之正常運轉及實驗進行之效率，MIR 目前對所有進行之動物相關實驗皆採付費制度，所有實驗人員皆須填寫相關實驗需求表，根據各項實驗進行所需之技術人員、人力及時間計算實驗費用其收費標準如表：

PI	Grant #	Service	Units /hours	Charge /unit	Total Charge
		microPET	1	200	
		Tech time	1	50	
		Data anal	1	57	
		Bio-D	1	50	
				Total	$

MIR microPET/Animal Facility 對內收費之價目表

**MIR 前並無對外服務，外界可經由合作研究計畫使用進行 microPET 研究。

5. 目前 MIR 的研究，使用核種主要是使用銅-64（Cu-64）、氟-18（F-18）及碳-11（C-11）。茲將分別敘述於下：第一部分銅-64（Cu-64）：Cu-64 主要應用於標幟體抑素類似物（somatostatin

peptide analogs)。化學家不斷研發此系列的新化合物，修飾（peptide）本身結構或改變螯合物（chelator），再以 Cu-64 放射性同位素標幟，進一步進行動物體生物活性實驗。目前該所使用的動物模式是將 AR42J 大鼠胰臟癌細胞種植在未成熟三週大的 Lewis rat 身上，選擇大鼠是因為大鼠的體積較大，於 microPET 造影上相對於小鼠會有較佳的解析度，此一動物模式已引入本所，用以進行相關同位素標幟體抑素動物實驗。第二部分是 Cu-64 標幟抗體，利用抗原-抗體(Antigen-Antibody)的特異性結合應用於免疫相關疾病之研究。有關 Cu-64 之臨床應用，目前只有在華盛頓大學進行相關試驗，尚無新藥上市。第三部分是氟-18（F-18）：主要是將 F-18 標幟於 Thymidine 使成 F-18-Fluorothymidine (FLT)，標幟 Acetate 成 F-18-Fluoroacetate (FAC)進行腫瘤動物模式之造影研究，同時與醫學院相關院所合作進行 F-18 標幟 FHBG 的基因治療研究。第四部分為碳-11（C-11），主要是進行 C-11-acatate 的合成，進行腫瘤造影探討，或 C-11-raclopride 多巴胺受體生物體結合造影研究，以利後續藥理機制及新藥開發的研究應用。

6. MIR 為有效進行研究工作，組成一個研究團隊，MIR 有許多負責與醫學院、醫院研究人員聯繫與

試驗規劃的研究員(Principal Investigator)，醫學院人員提供疾病之動物模式與資訊，MIR 的研究員瞭解 microPET 之應用與功能，負責實驗之規劃與設計，實驗結果之整理與醫院研究人員討論研究數據之生理、藥理意義，結果發表論文；為得到有意義之實驗數據，MIR 有三位技術熟練的動物實驗操作人員，一位 microPET 專職操作人員，兩位醫學物理背景的物理師負責實驗後 ROI 之圈選、數據計算與分析，一位研究員專職儀器維護與後續研發。就疾病動物模式之建立而言，必須藉由與外界醫院、醫學院合作來獲得，此為最有效率之方式。本次受訓瞭解 microPET 之最佳運作模式與儀器操作之基本技術與概念，有助於核研所 microPET 儀器之安裝與操作。

(八) 放射科學組 Anderson (Carolyn Anderson)教授實驗室主要研究題目之一為抑體素類似物(Somatostatin analogues)標幟 Cu-64 等不同放射性同位素，配合不同的螯合劑(Chelator)以發展造影與治療性核醫葯物，並已建立體外細胞及體內大白鼠動物分析模式，於國際著名核醫期刊發表許多卓越的研究成果，在此領域已具國際領導地位；張員與 Anderson 教授保持聯絡溝通其研究經驗，其實驗室目前著重於 peptide 之標幟研究除開發新的標幟方法外亦應用 microPET 來驗證其標

幟後之藥效。

(九) 本次實習參考該所各相關實驗室之擺設與規劃，尤其是 microPET 造影實驗室、Cu-64 標幟實驗室及 F-18 標幟實驗室；microPET 造影實驗室於 2002 年九月進行改裝，以因應 2003 年安裝之第二台 microPET，同時亦將再購入 microCT，以整合兩者之影像，進行 3D ROI(Region of Interest)之圈選與計算，該所規劃將二部 microPET 及 microCT 共同放置於同一間造影室，並由同一控制室控制。Cu-64 標幟實驗室(圖五-七)及 F-18 標幟實驗室(圖八-十二)皆有氣送管將射源及核醫藥物送至實驗室，以進行標幟實驗，因在此進行之實驗皆為細胞及動物實驗，目前各標幟實驗室標幟煙櫃皆未設置機械手臂以進行標幟，但設有許多自動化設備以減少操作人員之放射線暴露。

(十) 本次實習亦參與 microPET 動物實驗之進行，John 純熟的解剖操作技術令人印象深刻，microPET 因可用於動態造影(Dynamic Imaging)，因此必須使用氣體麻醉機，以保持實驗過程中小鼠保持麻醉，並製作各種壓克力模具，包含小鼠腦造影(圖十三)，腦造影壓克力模具(圖十四)，一隻小鼠造影模具(圖十五、圖十六)，一隻小鼠造影(圖十七)，兩隻小鼠壓克力模具(圖十八)及兩隻小鼠造影(圖十九、圖二十)相關實驗外，並採購相關器

材外，認識華盛頓大學的研究人員，建立未來聯繫管道，對核研所未來臨床前動物實驗之進行有很大幫助。實習期間並參觀該所硬體設備，以利本組建立其關鍵技術，收穫良多，華盛頓醫學院研究成果豐碩，其人力資源充裕，主要是具有技術成熟之實驗人員及博士後研究人員，建立許多關鍵技術，其 PET 中心迴旋加速器不斷生產與研製新的核醫藥物，作為臨床與研究用，並配合 microPET 之運作與研究。

四、建議:

(一) FLT 與 FAC 目前在國外已有許多研究在進行而在歐洲已有臨床試驗進行中，國內在人力與經費許可之下，未來此二種藥物之研究可考慮進行，以和 FDG 互相配合，使腫瘤造影診斷之種類更廣。在研究新藥同時，亦建議合作對象包含臨床醫師，藉由醫師從臨床應用之角度與影像判別之經驗使 mircoPET 研究更為完整。

(二) MIR 之 microPET 於 2000 年 12 月安裝，其運作的組織架構非常清楚，microPET 之運轉有專人負責儀器維護、操作，如此才能使機器每日穩定運轉，在實習期間，其儀器亦發生過數次問題，皆有賴專業的維護人員立即解決問題才能使機器再次操作，而專業操作人員能夠提供研究人員儀器的特性與性能，提供硬體維護人員儀器的近日狀況。就 microPET 的使用經驗而言，加州大學洛杉磯分校（UCLA）及華盛頓大學醫學院皆有專業人員的進行分工與整合。而目前 microPET 運作順利的團隊皆有完整之分工與制

度，張員初至該所實習時，Welch 博士及數位研究人員即提醒實習時間不長，其實無法進行完整的研究，要了解實習所學之優先度為何；他們建議實習目的在於學習其 microPET 運作制度及其經驗，將經驗帶回來，相關專業領域人員建立分工制度，並與華盛頓大學研究人員建立聯繫管道，做為核研所未來合作之橋樑。華盛頓大學實習之經驗，除瞭解所須之相關實驗與技術執行細節外，也瞭解其執行團隊之功能架構與分工，除學習馬林可研究所運作模式，再根據核研所之實際情形，將對核研所利用此項 microPET 儀器實驗之團隊，無論在技術上與分工合作上將有相當助益。就運作制度整體而言：

1. 就數據分析而言，目前運作方式是 Lori 配合實驗收集影像，後由 Kim 博士將影像數據進一步圈選 ROI，作定量分析。由於圈選結果之個人差異很大，甚至同一個人不同次圈選亦有差異，因此必須由同一人圈選計算，Kim 博士之背景為醫學物理，他共同負責 MIR 所有實驗之 ROI 之圈選與計算，使定量分析之誤差減至最小，核研所未

來可依其組織架構作分工，以達到儀器管理、數據分析與研究分工相互配合之目的。

2. 就 microPET 儀器而言，最重要是利用 ROI 圈選後進行定量分析，在應用於醫學研究與藥物開發，必須準確由得到的影像數據轉換成藥物濃度，而機器本身之狀態影響後續數據定量非常大，因此有賴專業同仁維持機器穩定，同時操作與管理人員必須按程序進行維護與校正，以保持研究之品質。

3. MIR 已利用 microPET 進行相當多實驗，並發表於著名期刊，其中由 Wang 博士與醫學院合作之利用進行自體免疫疾病研究，可以用影像很清楚看到自體免疫抗體在自靜脈注射入小鼠後在不同時間分佈至關節的情形，此既為應用於免疫學領域之研究的最佳例證之一，研究成果並發表於頂尖之期刊。核研所 microPET 目前已開始運轉，後必須加強與國內研究單位之合作，microPET 雖然必須用放射性同位素藥物，但不是只用於核醫藥物，它能運用於新藥開發、藥理研究及免疫學研究等等。

(三) 在實習過程中，亦與本所同仁保持聯絡，將相關的經驗及動物模式之建立傳回國內，使microPET 之研究可以同步進行，此一經驗可以在未來的人員實習中再加強，使研究工作與經驗獲得能夠同步進行。

(四) 馬林可研究所研究成果豐碩，主要的原因是擁有各方面專精的研究人員、技術人員，有人專精於細胞實驗方面，有人專精於動物方面，亦有人負責協助各研究室標準操作程序之撰寫與整合，在華盛頓大學醫學院中擁有許多博士生及來自美國其他大學的博士後研究員與各領域研究人員；由以上可知人員的素質與研究精神是一個單位成功的主要因素，正值轉型中的核研所應積極吸引未來年輕研究人員來所服務，以充實研究陣容。而目前核研所已有許多優秀的外聘年輕研究人員加入，為核研所帶來新的技術與經驗，也參與相關研究計劃，建議若他們參與之研究成果發表於國際會議，其優秀之外聘研究人員亦能擁有出國發表論文之機會，以鼓勵其研究風氣。

五、資料蒐集

(1) 華盛頓大學馬林可研究所 microPET 實驗室之相關表格。

(2) 華盛頓大學馬林可研究所 microPET 造影實驗室、Cu-64 標幟實驗室、F-18 標幟實驗室及動物造影實驗之相關照片。

(3) 華盛頓大學馬林可研究所 microPET 相關實驗之海報照片。

(4) F-18-Fluorothymidine (FLT) 之細胞吸收實驗與 F-18-Fluoroacetate (FAC) 之細胞代謝實驗之詳細實驗步驟與數據。

(5)代表性論文參考資料

1. Chatziioannou A. F., Cherry S. R., Shao Y., et al. Performance evaluation of microPET: a high-resolution lutetium oxyorthosilicate PET scanner for animal imaging. J Nucl Med 1999;40:1164-1175.

2. Chatziioannou A., Qi J., Moore A., et al. Comparison of 3-D maximum a posteriori and filtered backprojection algorithms for high-resolution animal imaging with microPET. IEEE Trans Med Imaging 2000;19:507-512.

3. Kaarstad K., Bender D., Bentzen L., Munk O. L.,Keiding S. Metabolic fate of 18F-FDG in mice bearing either SCCVII squamous cell carcinoma or C3H mammary carcinoma. J Nucl Med 2002;43:940-947.

4. Rigo P., Paulus P., Kaschten B. J., et al. Oncological applications of positron emission tomography with fluorine-18 fluorodeoxyglucose. Eur J Nucl Med Mol Imaging 1996;23:1641-1674.

5. Weber W.A., Avril N.,Schwaiger M. Relevance of positron emission tomography (PET) in oncology. Strahlenther Onkol 1999;175:356-373.

6. Findlay M, Young H., Cunningham D., et al. Noninvasive monitoring of tumor metabolism using fluorodeoxyglucose and positron emission tomography in colorectal cancer liver metastases: Correlation with tumor response to fluorouracil. J Clin Oncol 1996;14:700-708.

7. Schulte M., Brecht-Krauss D., Werner M., et al. Evaluation of neoadjuvant therapy response of osteogenic sarcoma using FDG PET. J Nucl Med 1999;40:1637-1643.

8. Wahl R.L., Zasadny K., Helvie M., et al. Metabolic monitoring of breast cancer chemohormonotherapy using positron emission tomography: Initial evaluation. J Clin Oncol. 1993;11:2101-2111.

9. Oyama N., Kim J., Jones L. A., et al. MicroPET assessment of androgenic control of glucose and acetate uptake in the rat prostate and a prostate cancer tumor model. Nucl Med Biol 2002;29:783-790.

10. Yang W.K. Et Al., 'Integrase' protein of murine ecotropic murine leukemia viruses. In: Wu CW, Wu F (eds). Structure and Function of Proteins and Nucleic Acids. 1990, New York: Raven Press.

11. Wang J., Yang W. K., Yang Y., et al. Paradoxical effect of GM-CSF gene transfer on the tumorigenicity and immunogenicity of murine tumors. Int J Cancer 1998;75:459-466.

12. Wei S. J., Chao Y., Shih Y. L., et al. Involvement of Fas (CD95/APO-1) and Fas ligand in apoptosis induced by ganciclovir treatment of tumor cells transduced with herpes simplex virus thymidine kinase. Gene Ther 1999;6:420-431.

13. Gambhir S. S., Barrio J. R., Wu L., et al. Imaging of adenoviral-directed herpes simplex virus type 1 thymidine kinase reporter gene expression in mice with radiolabeled ganciclovir. J Nucl Med 1998;39:2003-2011.

14. Hwang J. J., Liao M. H., Yen T. C., et al. Biodistribution study of [99mTc] TRODAT-1 alone or combined with other dopaminergic drugs in mice with macroautoradiography. Appl Radiat Isot 2002;57:35-42.

15. Gambhir S. S., Herschman H. R., Cherry S. R., et al. Imaging transgene expression with radionuclide imaging technologies. Neoplasia 2000;2:118-138.

16. Kornblum H. I.,Cherry S. R. The use of microPET for the development of neural repair therapeutics: studies in epilepsy and lesion models. J Clin Pharmacol 2001;Suppl:55S-63S.

17. Lewis J. S., Connett J. M., Garbow J. R., et al. Copper-64-pyruvaldehyde-bis(N(4)-methylthiosemicarbazone) for the prevention of tumor growth at wound sites following laparoscopic surgery: monitoring therapy response with microPET and magnetic resonance imaging. Cancer Res 2002;62:445-449.

18. Li W. P., Lewis J. S., Kim J., et al. DOTA-D-Tyr(1)-octreotate: a somatostatin analogue for labeling with metal and halogen radionuclides for cancer imaging and therapy. Bioconjug Chem 2002;13:721-728.

19. Ugur O., Kothari P. J., Finn R. D., et al. Ga-66 labeled somatostatin analogue DOTA-DPhe1-Tyr3-octreotide as a potential agent for positron emission tomography imaging and receptor mediated internal radiotherapy of somatostatin receptor positive tumors. Nucl Med Biol 2002;29:147-157.

圖一 B-J 醫院 (Barnes-Jewish Hospital)

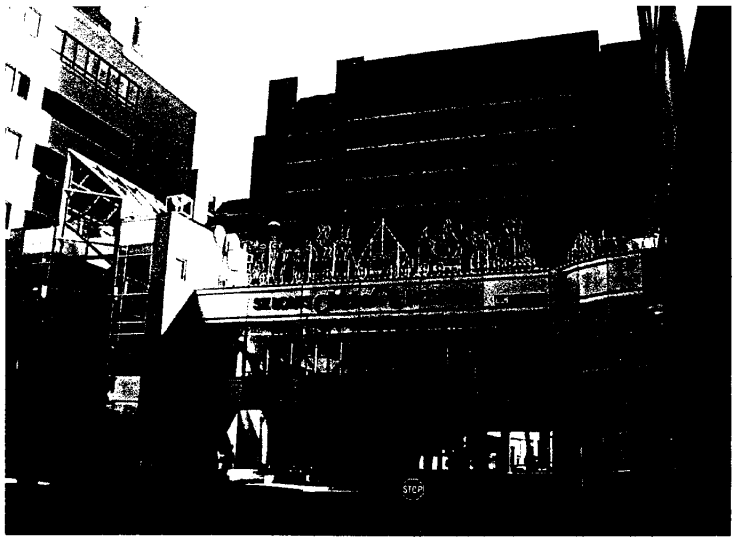

圖二 聖路易市兒童醫院(St.Louis Children Hospital)

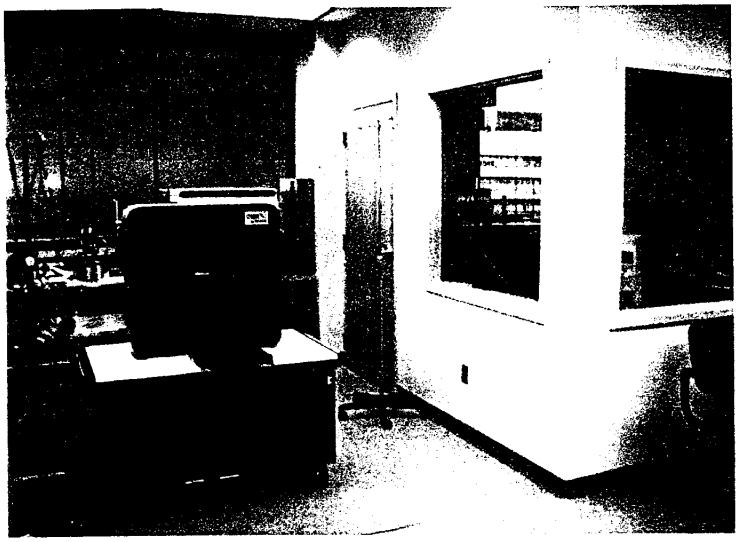

圖三 華盛頓大學 microPET 動物實驗室(I)

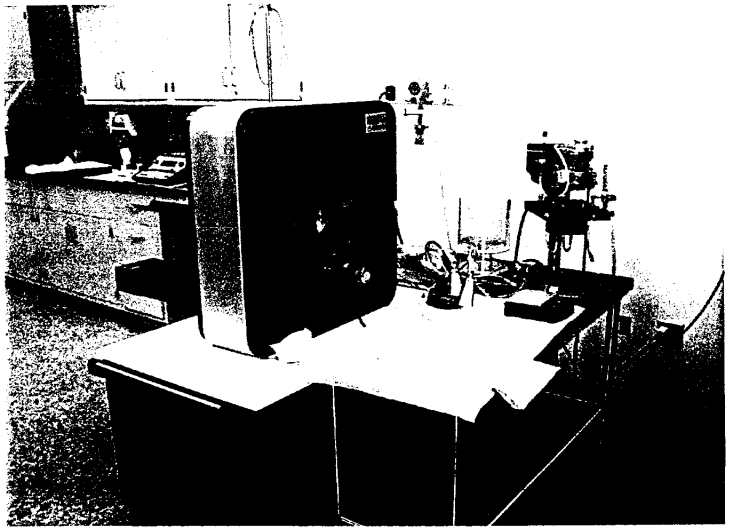

圖四 華盛頓大學 microPET 動物實驗室(II)

圖五 華盛頓大學 Cu-64 標幟實驗室(I)

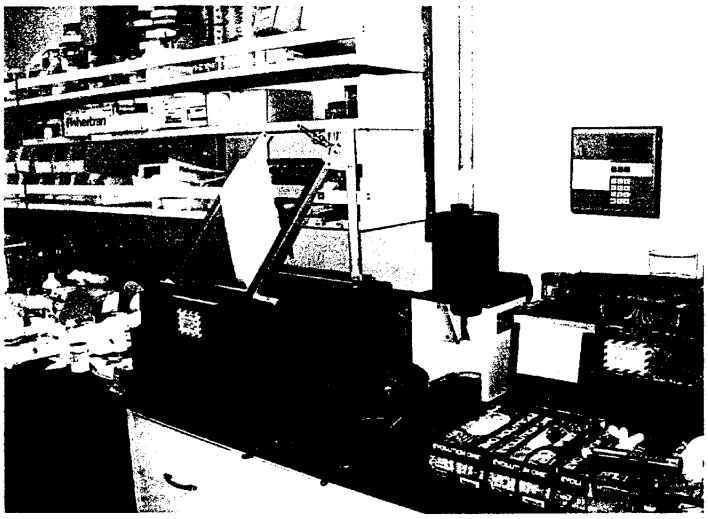

圖六 華盛頓大學 Cu-64 標幟實驗室(II)

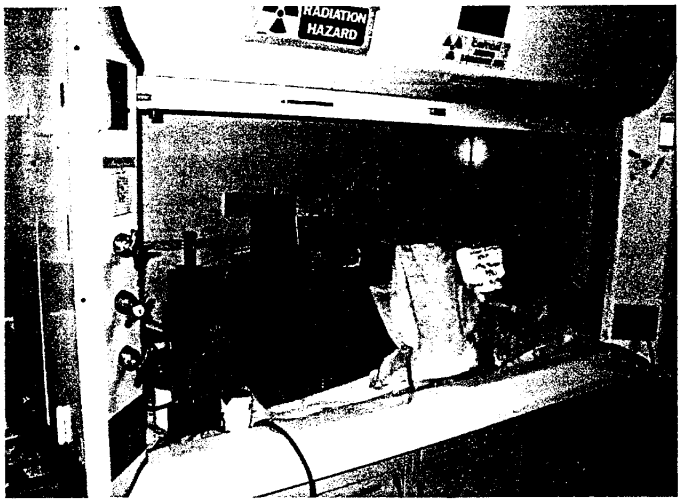

圖七 華盛頓大學 Cu-64 標幟實驗室(III)

圖八 華盛頓大學 F-18 標幟實驗室(I)

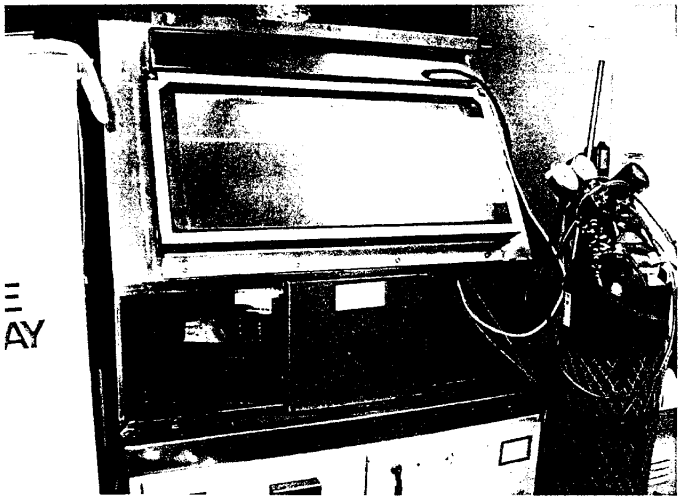

圖九 華盛頓大學 F-18 標幟實驗室(II)

圖十 華盛頓大學 F-18 標幟實驗室(III)

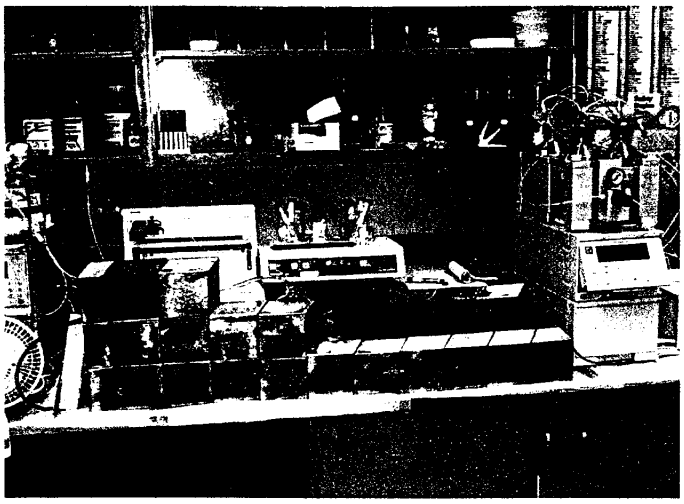

圖十一 華盛頓大學 F-18 標幟實驗室(IV)

圖十二 華盛頓大學 F-18 標幟實驗室(V)

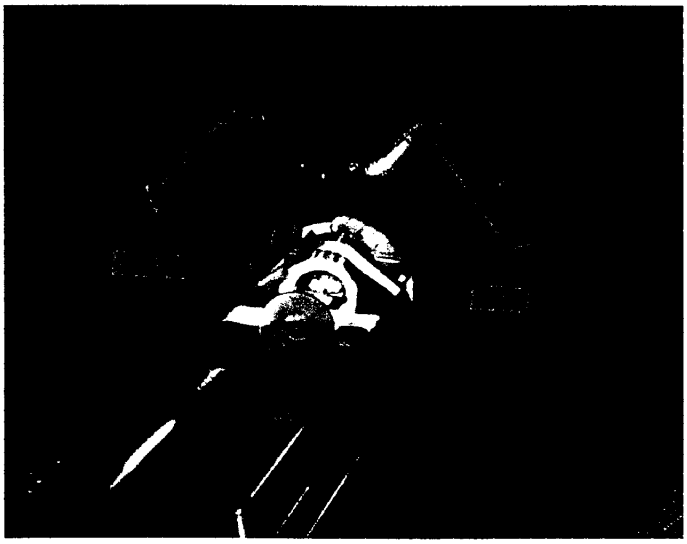

圖十三 小鼠腦造影

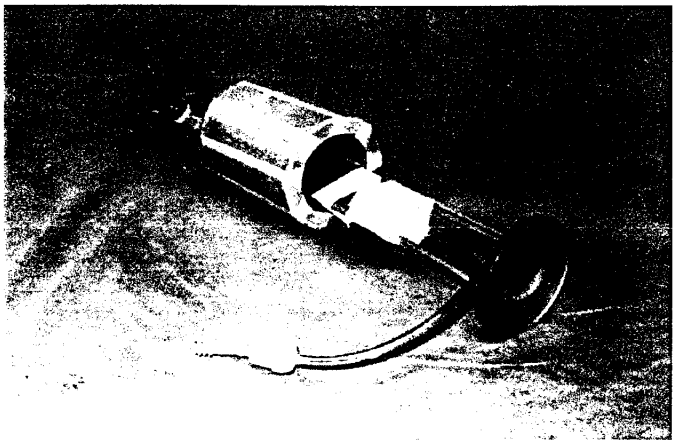

圖十四 腦造影壓克力模具

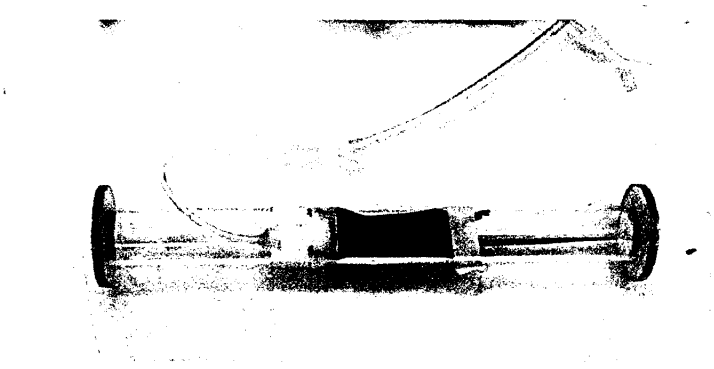

圖十五 一隻小鼠造影模具(I)

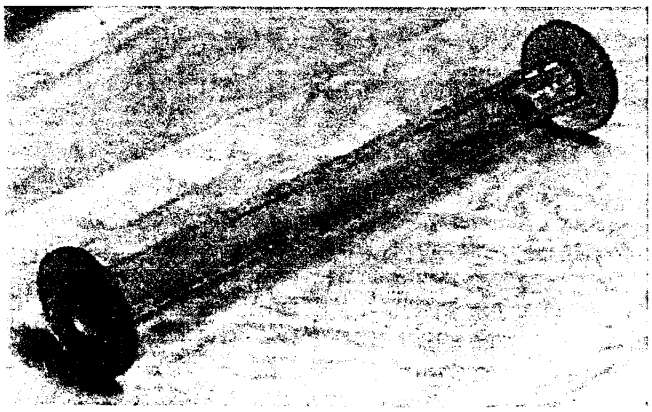

圖十六 一隻小鼠造影模具(II)

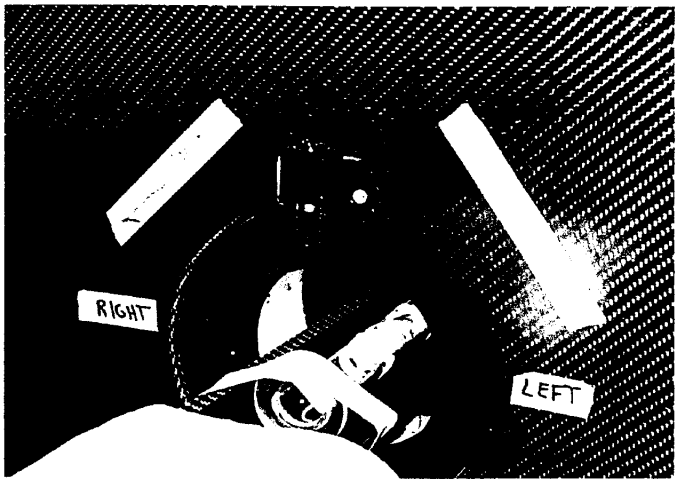

圖十七 一隻小鼠造影

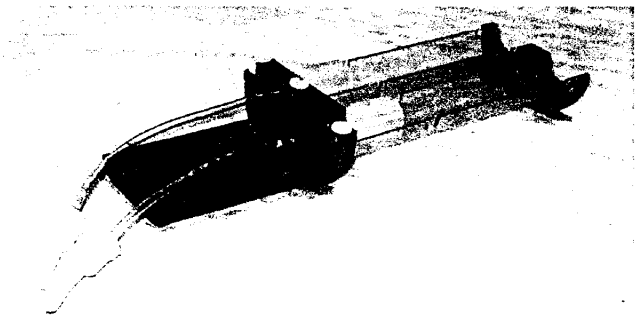

圖十八 兩隻小鼠壓克力模具

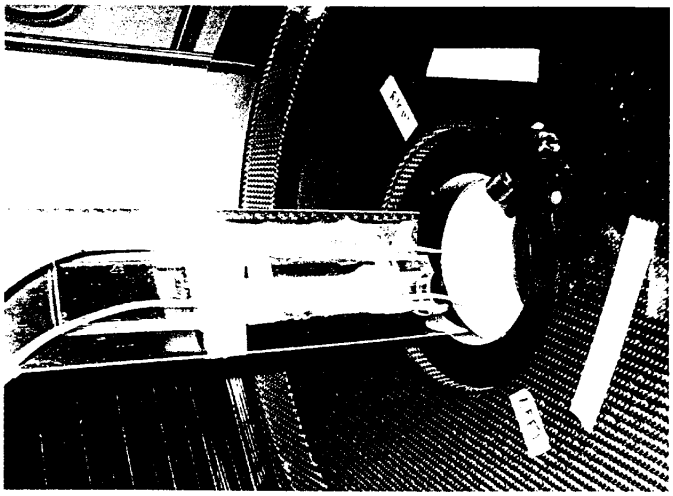

圖十九 兩隻小鼠造影(I)

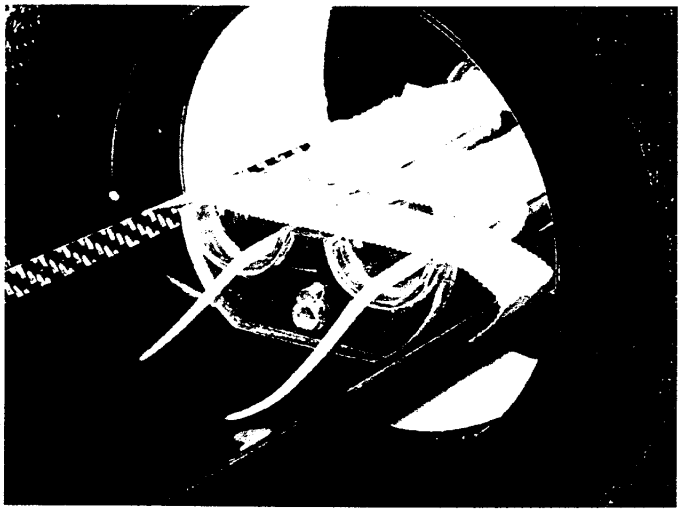

圖二十 兩隻小鼠造影(II)

附錄：

華盛頓大學醫學院馬林可研究所 2002 年發表之

重要 microPET 論文

ELSEVIER

Nuclear Medicine and Biology 29 (2002) 783–790

NUCLEAR MEDICINE — AND — BIOLOGY

www.elsevier.com/locate/nucmedbio

MicroPET assessment of androgenic control of glucose and acetate uptake in the rat prostate and a prostate cancer tumor model

Nobuyuki Oyama, Joonyoung Kim, Lynne A. Jones, Nicole M. Mercer, John A. Engelbach, Terry L. Sharp, Michael J. Welch*

Division of Radiological Sciences and the Alvin J. Siteman Cancer Center, Mallinckrodt Institute of Radiology, Washington University School of Medicine, Saint Louis, Missouri, USA

Received 21 May 2002; received in revised form 5 July 2002; accepted 12 July 2002

Abstract

PET has been used to monitor changes in tumor metabolism in breast cancer following hormonal therapy. This study was undertaken to determine whether PET imaging could evaluate early metabolic changes in prostate tumor following androgen ablation therapy. Studies were performed comparing two positron-emitting tracers, ^{18}F-FDG and ^{11}C-acetate, in Sprague-Dawley male rats to monitor metabolic changes in normal prostate tissue. Additional studies were performed in nude mice bearing the CWR22 androgen-dependent human prostate tumor to evaluate metabolic changes in prostate tumor. In rats, for the androgen ablation pretreatment, 1 mg diethylstilbestrol (DES) was injected subcutaneously 3 and 24 hours before tracer injection. For androgen pretreatment, 500 μg dihydrotestosterone (DHT) was injected intraperitoneally 2 and 6 hours before tracer injection. The rats were divided into three groups, Group A (no-DES, no-DHT, n = 18), Group B (DES, no-DHT, n = 18) and Group C (DES, DHT, n = 18). In each group, 10 animals received ^{18}F-FDG, whereas the remaining eight animals were administered ^{11}C-acetate. Rats were sacrificed at 120 min post-injection of ^{18}F-FDG or 30 min post-injection of ^{11}C-acetate. Pretreatment of the mouse model using DHT (200 μg of DHT in 0.1 mL of sunflower seed oil) or DES (200 μg of DES in 0.1 mL of sunflower seed oil) was conducted every 2 days for one week. Mice were imaged with both tracers in the microPET scanner (Concorde Microsystems Inc.). DES treatment caused a decrease in acetate and glucose metabolism in the rat prostate. Co-treatment with DHT maintained the glucose metabolism levels at baseline values. In the tumor bearing mice, similar effects were seen in ^{18}F-FDG study, while there was no significant difference in ^{11}C-acetate uptake. These results indicate that changes in serum testosterone levels influence ^{18}F-FDG uptake in the prostate gland, which is closely tied to glucose metabolism, within 24 hours of treatment and in the prostate tumor within 1 week. These early metabolic changes could enable monitoring metabolic changes in prostate tumor following treatment by imaging using ^{18}F-FDG PET. Further studies are needed to clarify the reason for the insensitivity of ^{11}C-acetate for measuring metabolic change in prostate tumor.

Keywords: Positron emission tomography; Prostate cancer; Androgen dependency; Tumor metabolism; MicroPET

1. Introduction

Prostate cancer is the most commonly diagnosed cancer and is the second leading cause of cancer death in men over the age of 40 years in the United States [2]. Most prostate cancers show androgen dependency for growth at presentation [4], hence androgen ablation therapy is a major treatment for patients with advanced disease. However, approximately 50% of those patients receiving androgen ablation therapy relapse within one year, while others respond to therapy for extended periods. This varied response to the therapy indicates that there are large differences in the androgen dependency of prostate cancer patients. To achieve a greater response rate for patients with less androgen dependent cancer, combination therapies with radiotherapy or chemotherapy are often explored. To select these patients, serum prostate specific antigen (PSA) values or prostate volume estimated by computed tomography (CT) or ultrasonography (US) are employed to monitor the effect of androgen ablation therapy. These methods often take 1 to 3 months after the initiation of treatment for the first accurate assessment to be made. A more rapid evaluation method would allow androgen ablation therapy to be used only on patients who will respond to this treatment.

* Corresponding author. Tel.: +1-314-362-2809; fax: +1-314-362-2806.

E-mail address: welchm@mir.wustl.edu (M.J. Welch).

0969-8051/02/$ – see front matter
PII: S0969-8051(02)00346-3

Evaluation of tumor metabolism by positron-emission tomography (PET) is a relatively new procedure for assessing the early effects for cancer therapy and has already been applied to breast cancer [1]. This study showed that the efficacy of tamoxifen therapy could be predicted by measuring the agonist flare response using 2-[^{18}F] fluoro-2-deoxy-D-glucose (^{18}F-FDG) in a short time period (7–10 days). Prostate cancer shows hormone dependency in a manner similar to breast cancer, whereas tumor metabolism of androgen dependent prostate cancer is thought to be influenced by serum testosterone levels. Thus, this study was designed to determine whether PET imaging could detect early changes in tumor metabolism following androgen ablation therapy.

2. Materials and methods

2.1. Radiochemical synthesis

^{18}F-fluoride is produced via the ^{18}O(p, n) ^{18}F nuclear reaction by irradiating isotopically enriched ^{18}O-water with 15–16 MeV protons using either the Washington University Cyclotron Corporation CS-15 or the Japan Steel Works (JSW) BC-16/8 medical cyclotron located in the MIR Cyclotron Facility. ^{18}F-FDG was prepared using the Coincidence Technologies ^{18}F-FDG synthesis module. This method of preparation is based on the methods of Hamacher et al. [3]. ^{11}C-carbon dioxide will be produced via the ^{14}N(p, α) ^{11}C reaction. Targets are installed on the beam lines of both the Washington University JSW-16/8 Cyclotron, CS-15 cyclotron and the RD 111 cyclotron. ^{11}C-acetate was prepared by the reaction of ^{11}C-labeled carbon dioxide with the appropriate Grignard reagent as described previously [6].

2.2. Biodistribution studies

2.2.1. Normal rat prostate study

All animal handling was performed in accordance with Washington University in St. Louis, Occupational Health and Safety guidelines. Animal experiments were conducted in compliance with the Guidelines for the Care and Use of Research Animals established by the Animal Studies Committee at our institution. Mature male Sprague-Dawley rats (160–200 g) were either untreated or pretreated with diethylstilbestrol (DES) to suppress endogenous androgen synthesis. The treated animals were injected subcutaneously with 1 mg DES in 0.2 mL of sunflower seed oil at 24 hr and 3 hr prior to the study, following methods of Symes [13]. Half of the DES treated animals were also treated with dihydrotestosterone (DHT). They were injected intraperitoneally with 500 μg of DHT in 1.5 mL of 20% EtOH at 2 hr and 6 hr prior to the experiment. The animals were fasted overnight prior to ^{18}F-FDG or ^{11}C-acetate injection. The animals were injected intravenously with 20 μCi of ^{18}F-FDG or 50 μCi of ^{11}C-acetate via the tail vein under isoflurane anesthesia. At the specified time points, the animals were sacrificed, samples of blood and tissue were excised, weighed and the radioactivity determined in a Beckman Gamma 8000 as previously reported [5]. The injected dose was calculated from standards prepared from the injection solution, and the data were expressed as percent injected dose per gram of tissue (%ID/g).

2.2.2. Tumor model study

Four- to six-week-old athymic nu/nu male mice were obtained from Charles River Laboratories. The CWR22 tumor line was a gift from Dr. Pretlow (Case Western Reserve University, Cleveland, OH). The CWR22 tumor was propagated in the animals by the implantation of minced tumor tissue from a previously established tumor into the subcutaneous tissue of the flanks of the mice. For the maintenance of high serum androgen levels, mice were implanted with 12.5 mg of 60-day-releasing testosterone pellets (Innovative Research of America, Sarasota, FL) subcutaneously. In mice, for the androgen ablation pretreatment, testosterone pellets were removed and 200 μg of DES in 0.1 mL of sunflower seed oil was injected subcutaneously every two days for one week. For androgen treatment, 200 μg DHT in 0.1 mL of sunflower seed oil was injected subcutaneously every two days for one week. For control mice, 0.1 mL of sunflower seed oil was injected subcutaneously every two days for one week. After the treatment, the mice were injected intravenously with 20 μCi of ^{18}F-FDG or 50 μCi of ^{11}C-acetate via tail vein. At the specified time points, 0.5 hr for ^{11}C-acetate and 1 hr for ^{18}F-FDG, the animals were sacrificed, samples of blood and tissue were excised, weighed and the activity concentration determined. The injected dose was calculated from standards prepared from the injection solution, and the data were expressed as percent injected dose per gram of tissue (%ID/g).

2.3. MicroPET imaging

Approximately six weeks after tumor implantation, two CWR22 tumor bearing-mice were imaged simultaneously in the prone position in the microPET scanner (Concorde Microsystems, Knoxville, TN) for the baseline PET scans. Mice were first anesthetized with 1–2% isoflurane and placed in the prone position in a custom-designed holder that allows simultaneous imaging of two mice. The entire holder was placed near the center of field of view (CFOV) of the microPET scanner where the highest image resolution and sensitivity are available. Dynamic imaging was performed for 60 minutes starting at the injection of 500 μCi of ^{11}C-acetate to each mouse via micro-catheter (Harvard Apparatus, Inc) placed in their external jugular veins. The frame durations were defined as followings: 5 sec/frame × 24 frames, followed by 10 sec/frame × 10 frames, followed by 20 sec/frame × 10 frames, followed by 150 sec/frame × 2 frames, followed by 300 sec/frame × 4 frames. Following

Table 1
Biodistribution of ^{18}F-FDG in rats (n = 10) at 2 hour (%ID/g ± SD)

Tissue	Control	DES	DES+DHT
Blood	0.14 ± 0.03	0.13 ± 0.02	0.11 ± 0.02
Lung	0.46 ± 0.06	0.47 ± 0.04	0.39 ± 0.03
Liver	0.19 ± 0.03	0.21 ± 0.02	0.18 ± 0.02
Muscle	0.10 ± 0.01	0.10 ± 0.01	0.11 ± 0.04
Prostate(v)[a]	0.94 ± 0.26*	0.52 ± 0.26*	1.02 ± 0.78
Prostate(d)[b]	0.88 ± 0.24**	0.47 ± 0.19**	0.71 ± 0.46

[a]: v = ventral, [b]d = dorsolateral, *: p = 0.003, **: p = 0.001 (Mann-Whitney Test).

Table 3
Biodistribution of ^{18}F-FDG in mice (n = 10) bearing CWR22 tumor xenograft at 1 hour (%ID/g ± SD)

Tissue	Control	DES	DHT
Blood	0.53 ± 0.10	0.65 ± 0.10	0.68 ± 0.17
Lung	2.36 ± 0.48	2.74 ± 0.42	2.42 ± 0.47
Liver	0.89 ± 0.18	1.40 ± 0.32	1.06 ± 0.22
Muscle	1.70 ± 0.56	1.81 ± 0.87	2.61 ± 1.08
Prostate	1.75 ± 1.24	1.91 ± 0.42	1.41 ± 0.37
Tumor	2.35 ± 0.53*	1.40 ± 0.10*	2.62 ± 0.41

* : p = 0.015 (Mann-Whitney Test).

^{11}C-acetate-microPET, 500 μCi of ^{18}F-FDG was injected into the same mice. A 10-min static scan was obtained one-hour post ^{18}F-FDG injection. After these initial baseline PET scans, the mice were treated with either DHT or DES every two days for one week as described above. On day 7, microPET imaging was repeated with the same protocol as described for the baseline studies. All raw data were first sorted into 3-dimensional (3D) sinograms, followed by Fourier Rebinning and 2D Filtered Back-Projection (FBP) reconstruction using Ramp filter with one half of the Nyquist frequency as the cut-off frequency. A region of interest (ROI) was placed on the organ or tumor of interest in the transaxial microPET images that include the entire tumor or organ volume. The average radioactivity concentration within a tumor or an organ was obtained from the average pixel values within the multiple ROI volume. To eliminate the dependency on the injected activity, an uptake index of a tumor or an organ was defined as the average radioactivity concentration divided by the total injected activity with the following formula:

Uptake index = average radioactivity concentration in ROI (μCi/μL)/injected dose (μCi)

The uptake index of ^{11}C-acetate and ^{18}F-FDG in each tumor were compared before and after the treatment. From the ^{11}C-acetate dynamic study, time activity curves (TAC) were also calculated from the uptake index of the tumor. In these microPET scans, the attenuation corrections were not applied, because the accuracy of the measured attenuation correction was poor with this scanner and also the amount of attenuation from a mouse body was relatively small and the shape of mouse body did not change significantly between different subjects. Instead, the attenuation correction factors were incorporated into the system calibration. To be briefly described, a small vial with similar volume (24 mL) to a mouse body was used. The vial was filled with ^{18}F-FDG of known concentration and scanned for at least half an hour. Images were reconstructed with standard protocol and the ROI were drawn from the central ten image planes enclosing at least 90% of the cross-section of the vial. These ROI included regions close to the surface, as well as at the center, of the vial. The average pixel value was then compared to the known activity concentration to obtain the system calibration factor. This approach was validated by drawing additional ROIs that were either near the surface of the vial or at the very center. None of them deviated from the average values by more than 10%, and most were within the 5% range. With this approach, a mouse study had a quantitative accuracy of less than 10% in error, regardless of whether the ROI is superficial or deep within the mouse body. The partial volume effect in estimating the ROI values from microPET images were small in these PET scans because implanted tumors were more than 1 cm in diameter, which was well above the resolution limit of this microPET system [14].

Table 2
Biodistribution of ^{11}C-Acetate in rats (n = 8) at 30 min (%ID/g ± SD)

Tissue	Control	DES	DES+DHT
Blood	0.20 ± 0.04	0.21 ± 0.02	0.21 ± 0.04
Lung	0.49 ± 0.10	0.42 ± 0.07	0.44 ± 0.01
Liver	0.40 ± 0.05	0.43 ± 0.03	0.43 ± 0.05
Muscle	0.17 ± 0.04	0.18 ± 0.02	0.18 ± 0.03
Prostate(v)	0.32 ± 0.07*	0.22 ± 0.06*	0.25 ± 0.05
Prostate(d)	0.31 ± 0.08**	0.22 ± 0.07**	0.24 ± 0.05

* : p = 0.008, **: p = 0.029 (Mann-Whitney Test).

2.4. Statistical evaluation

Biodistribution data are reported as the mean ± the sample standard deviation (SD) for %ID/g. The Mann-Whitney U-test was used to compare tracer uptake before and after the treatments. Statistical significance was established at $p < 0.05$.

Table 4
Biodistribution of ^{11}C-Acetate in mice (n = 8) bearing CWR22 tumor xenograft at 30 min (%ID/g ± SD)

Tissue	Control	DES	DHT
Blood	0.41 ± 0.02	0.52 ± 0.05	0.39 ± 0.10
Heart	0.79 ± 0.31	0.76 ± 0.23	0.37 ± 0.03
Liver	0.98 ± 0.08	1.22 ± 0.12	0.90 ± 0.06
Muscle	0.57 ± 0.21	0.70 ± 0.05	0.41 ± 0.16
Prostate*	0.25 ± 0.15	0.28 ± 0.11	0.39 ± 0.23
Tumor**	0.88 ± 0.21	1.21 ± 0.18	1.12 ± 0.24

*, **: N.S. (Mann-Whitney Test).

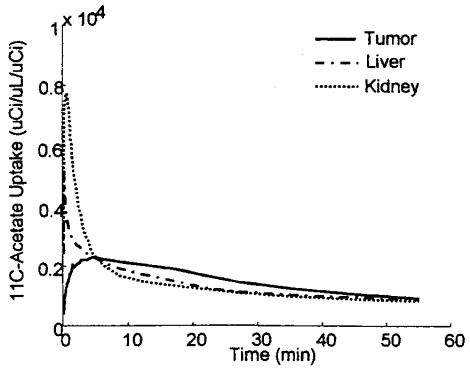

Fig. 1. Time activity curves for kidney (. . . . .), liver (– · – ·) and tumor (—) of CWR 22 tumor bearing mouse. Both kidney and liver show rapid clearance of tracer, while prostate tumor shows relative retention of tracer.

3. Results

3.1. Normal rat prostate study

For in vivo uptake studies, in order to suppress in vivo androgen biosynthesis, rats were treated with 1 mg of DES in 0.2 mL sunflower oil per rat, at 3 hr and 24 hr prior to injection of ^{18}F-FDG and ^{11}C-acetate. Biodistribution at 2 hr was performed with ^{18}F-FDG (Table 1). Biodistribution of ^{11}C-acetate was performed at 30 min (Table 2). The biodistribution results of ^{18}F-FDG indicate that androgen ablation (DES treatment) caused a decrease of ^{18}F-FDG uptake in prostate, with DHT recovering this change in ^{18}F-FDG uptake. Biodistribution results of ^{11}C-acetate shown in Table 2 also indicate that the DES treatment caused a decrease in ^{11}C-acetate uptake in normal rat prostate.

3.2. Tumor model study

Biodistribution at 1 hr was performed with ^{18}F-FDG (Table 3). Biodistribution of ^{11}C-acetate was performed at 30 min (Table 4). ^{18}F-FDG uptake into tumor of DES treated mice was 1.40 ± 0.10%ID/g, compared to 2.35 ± 0.53%ID/g and 2.62 ± 0.41%ID/g for no treatment and DHT treatment mice, respectively ($p = 0.015$). The biodistribution study using ^{18}F-FDG indicated that DES treatment caused a decrease in ^{18}F-FDG uptake in prostate tumor, with DHT recovering this change in ^{18}F-FDG uptake (Table 3). On the other hand, biodistribution results of ^{11}C-acetate indicated that the change in acetate uptake in the prostate tumor was not significant in the androgen ablation mice (Table 4).

3.3. Micropet study

Dynamic imaging was performed 60 min after ^{11}C-acetate injection. A region of interest (ROI) was placed on each tumor and other organs of interest in the transaxial micro-PET images. A time activity curve (TAC) was generated from each ROI (Fig. 1). In the liver, ^{11}C-acetate uptake reached its plateau within a few minutes after injection, with 40% of radioactivity remaining 30 min post injection. In the kidney, ^{11}C-acetate uptake reached its plateau within a few minutes after injection, with only 20% of radioactivity remaining 30 min post injection. In tumor, ^{11}C-acetate uptake reached its plateau within 10 minutes after injection, with 70% of radioactivity remaining 30 min post injection. Following analysis of the data using ROI and TAC, it was evident that a static scan 30–40 min post injection supplied images of sufficient contrast for future studies. Coronal images of microPET using both ^{11}C-acetate and ^{18}F-FDG clearly indicated tumors implanted in the left flank (Fig. 2). The microPET images demonstrated that there was no clear change of ^{11}C-acetate uptake into prostate tumor before and after DHT or DES treatment (Fig. 3). Following ^{11}C-acetate-microPET, ^{18}F-FDG was injected into the same mice. A 10-min static scan was obtained one-hour post ^{18}F-FDG injection. DES treatment caused a decrease in FDG uptake in the CWR22 prostate cancer, while there were no large differences in DHT treatment (Fig. 4). ROI analysis indicated no significant change in ^{11}C-acetate uptake in either the tumors following DHT of DES treatment, or in the control group (Fig. 5). In the ^{18}F-FDG studies, tracer uptake showed no significant differences after DHT treatment, but tracer uptake did decrease from 15.72 to 6.60 (nCi/cc/μCi) after DES treatment ($p<0.001$), versus a decrease from 19.78 to 15.12 (nCi/cc/μCi) in the control group ($p<0.001$) (Fig. 6).

4. Discussion

There is a need to find better ways to distinguish between patients with prostate cancers who show poor prognosis from those who show better prognosis. In patients with localized disease receiving prostatectomy, Gleason grade, cancer volume, positive lymph node findings, and intraprostatic vascular invasion were independently associated with cancer progression [12]. Most patients receiving androgen ablation therapy show advanced clinical stage at initiation of therapy. In this patient group, it would be ideal to know the differences in androgen dependency for each individual patient in order to use additional therapies in patients with cancers showing weak androgen dependency. For this purpose, most urologists follow the change of serum PSA values or total prostate volume every few months to monitor the cancers response to therapy. The LH-RH (luteinizing hormone–releasing hormone) agonist is one of the most popular agents for androgen ablation therapy for advanced

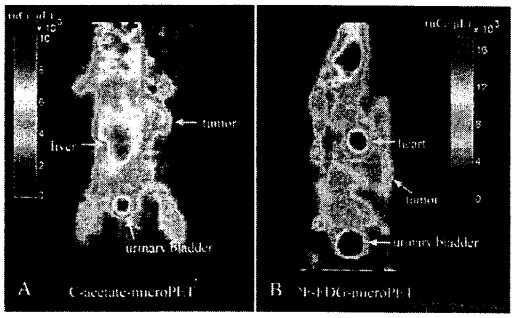

Fig. 2. (A) Coronal images of ^{11}C-acetate microPET of the mouse before treatment. (B) Coronal images of ^{18}F-FDG microPET of the mice before treatment.

prostate cancer disease. This LH-RH agonist leads to a suppression of LH and of testosterone productions equivalent to castration levels, leading to decline of positive stimulation via androgen receptors (AR) for cancer growth, followed by suppression of tumor growth. However, this peptide stimulates LH release, causing an initial flare of serum testosterone during the first 2 to 3 weeks associated with rise in PSA. As a result, it takes a few months for the first accurate assessment of androgen ablation therapy.

To assess the therapeutic effect of androgen ablation therapy, other kinds of imaging modalities have been studied for diagnosis of prostate cancer. It was reported that MRS (magnetic resonance spectroscopic) imaging combined with MRI was used to study the therapeutic effects of

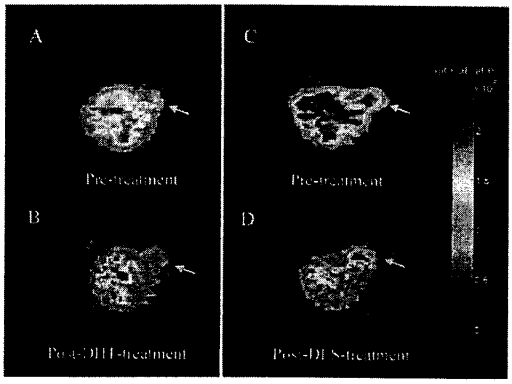

Fig. 3. (A, B) MicroPET images showing ^{11}C-acetate uptake in the same tumor-bearing mouse before and after DHT treatment. (A) MicroPET showed ^{11}C-acetate uptake in tumor before treatment. (B) After one week DHT treatment, ^{11}C-acetate uptake showed almost no change. (C, D) MicroPET showing ^{11}C-acetate uptake in the same tumor-bearing mouse before and after DES treatment. (C) MicroPET showed ^{11}C-acetate uptake in tumor before treatment. (D) After one week DES treatment, ^{11}C-acetate uptake showed almost no change.

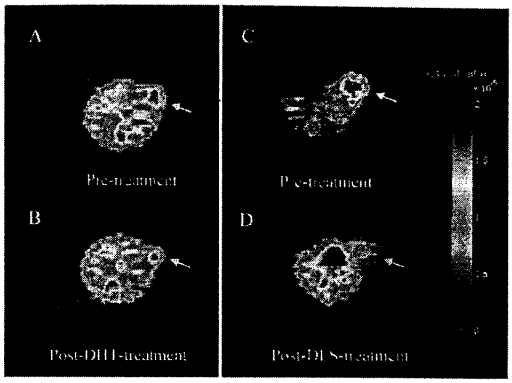

Fig. 4. (A, B) MicroPET images showing ^{18}F-FDG uptake in the same tumor-bearing mouse before and after DHT treatment. (A) MicroPET showed ^{18}F-FDG uptake in tumor before treatment. (B) After one week DHT treatment, ^{18}F-FDG uptake showed almost no change. (C, D) MicroPET showing ^{18}F-FDGuptake in the same tumor-bearing mouse before and after DES treatment. (C) MicroPET showed ^{18}F-FDG uptake in tumor before treatment. (D) After one week DES treatment, ^{18}F-FDG uptake was largely decreased.

therapy in 65 patients with prostate cancer to provide both a measure of cancer and a time-course of metabolic response following androgen ablation therapy [8]. ^{11}C-choline has also been proposed as a new radiopharmaceutical for the imaging of prostate cancer with PET, not only for cancer detection but also for estimating the effectiveness of cancer therapy [7]. These are preliminary reports, and more data will be needed to confirm the usefulness of these imaging modalities for this purpose.

Recently, ^{18}F-FDG PET has demonstrated its clinical value in demonstrating tumor metabolism. Oyama, et al. reported that ^{18}F-FDG uptake in prostate cancers was suppressed by androgen ablation after 1 to 3 months [10]. However, the early effects of androgen ablation within a month from initial therapy to cancer metabolism of the prostate is still unknown, and may be useful in evaluating the early effects of cancer therapy. In this current study we measured the early changes in the tissue metabolism of the normal prostate gland and prostate cancer tissue caused by androgen ablation treatment using an in vivo animal model. In our recent study, we also reported that ^{11}C-acetate PET imaging shows high sensitivity for detection of primary as well as distant metastatic prostate cancer lesions [9].

The biodistribution studies (Table 1, 2) showed that androgen ablation caused a decrease of ^{18}F-FDG uptake in the prostate, with DHT administration returning its uptake to that of the baseline level. This clearly indicates that serum testosterone levels influence glucose metabolism in the prostate. Moreover, the decline of ^{18}F-FDG uptake was detected within 24 hr after initiation of androgen ablation. ^{18}F-FDG is a promising tracer to evaluate changes in prostate metabolism, and it will contrib-

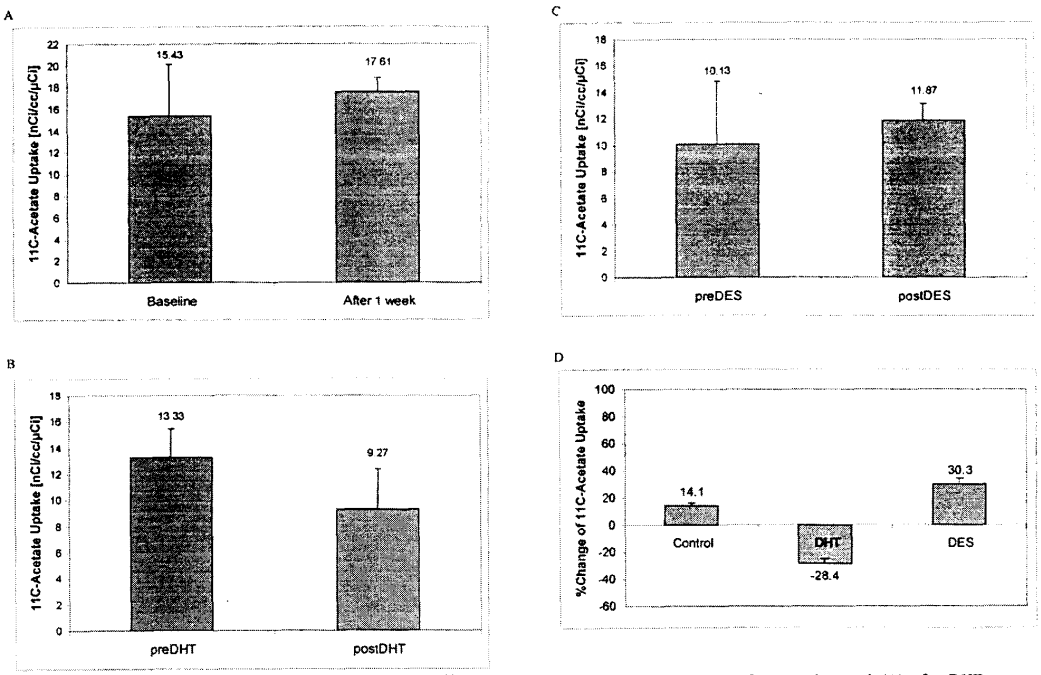

Fig. 5. (A) In ROI analysis, there was no significant difference in ^{11}C-acetate uptake in tumor in control mice after 1-week-growth (A), after DHT treatment (B) and after DES treatment (C). (D) Average change of ^{11}C-acetate uptake in tumor was +30.3% in DES group, -28.4% in DHT group. Data are the mean and standard deviation of the mice in each group.

ute to predict androgen dependency of prostate cancer in early phase of androgen ablation therapy. Additionally, the decrease of ^{11}C-acetate uptake in the prostate after androgen ablation was also significant in this study. The mechanism of high ^{11}C-acetate accumulation in tumor cells is uncertain, however it is thought to be different from that of the myocardium. Yoshimoto et al. studied uptake of ^{14}C-acetate in four tumor cell lines and a fibroblast cell line to investigate the metabolic pathway of ^{11}C-acetate in tumor cells [15]. They showed that ^{14}C accumulation in the four tumor lines was higher than that in fibroblast and this accumulation in tumor cells was due to enhanced lipid synthesis. Given the highly active basal lipid metabolism associated with the cell membrane because of tumor growth, ^{11}C-acetate may be an important proof of this anabolic pathway of metabolism in cancer tissue.

In the biodistribution studies using tumor-bearing mice, there were no significant changes in ^{11}C-acetate and ^{18}F-FDG uptake into prostate after DES or DHT treatment. The differences in acetate and glucose metabolism between mice and rats are unknown. The mice were injected with DHT or DES every 2 days for 1 week, and the last treatment was performed 1 day before sacrifice. The rats were treated with DHT 2 hour before and with DES 3 hour before sacrifice. The different administration times of DHT or DES might have contributed to the differences between the rats and mice studies.

In the current study we have also measured the early changes in the tissue metabolism of prostate cancer caused by androgen ablation treatment using an in vivo tumor model. The microPET study demonstrated that androgen ablation caused a decrease in ^{18}F-FDG uptake in prostate tumor, while additional DHT administration kept ^{18}F-FDG uptake in tumor to control levels. This clearly showed that serum testosterone levels influence glucose metabolism in androgen dependent prostate cancer. We also investigated the change of ^{11}C-acetate uptake into CWR22 tumor before and after DES or DHT treatment, however, there was no significant difference between them compared with normal rat prostate study. The reason for the insensitivity of ^{11}C-acetate for metabolic change in prostate tumor is not clear. One week of androgen ablation therapy might not be long enough to see changes in lipid metabolism in tumor cells investigated by biodistribution or microPET studies. Another possible reason for this lack of sensitivity of ^{11}C-acetate might be due to some inherent differences in ^{11}C-acetate

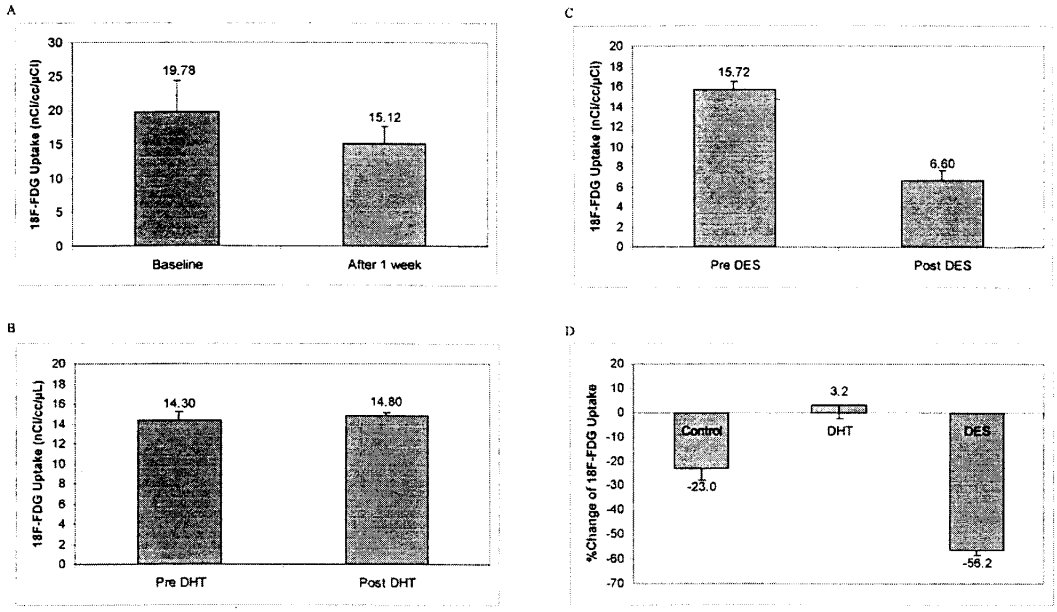

Fig. 6. (A) In ROI analysis, ^{18}F-FDG uptake in the tumor decreased in control group after 1-week-growth ($p < 0.001$). (B) There was no large difference in ^{18}F-FDG uptake in the tumor after DHT treatment. (C) There was large decrease of ^{18}F-FDG uptake in the tumor after DES treatment. With DES treatment, ^{18}F-FDG uptake largely decreased ($p < 0.001$). (D) Average change of ^{18}F-FDG uptake in the tumor was −58.2% in DES group, showing a greater decrease in ^{18}F-FDG than that of control group (−23.0%). Data are the mean and standard deviation of the mice in each group.

uptake in tumor at extended time points, although these time points are inappropriate for ^{11}C-acetate PET because of its short half-life.

In our microPET tumor model study, we did not observe any differences in ^{11}C-acetate and ^{18}F-FDG uptake into tumors between pre- and post-DHT treatment. We used male nude mice for this study and implanted testosterone-releasing pellets into mice prior to tumor implantation to increase the speed of tumor growth. Therefore, serum testosterone levels might not be high enough to enhance tumor-growing activity. In the results, additional DHT-treatment did not affect prostate tumor enough to increase tumor growth.

5. Conclusion

These findings confirm that ^{18}F-FDG is a promising tracer to evaluate changes in tumor metabolism, and may be able to predict the androgen dependency of prostate cancer in the early phase of androgen ablation therapy. These results indicate that changes in serum testosterone levels influence glucose metabolism in the prostate cancer within a week of treatment in mice and that it is possible to measure these changes using ^{18}F-FDG-microPET. These encouraging results will likely lead to human trials in the near future. This work is an example of how the microPET can be useful in evaluating the effects of specific cancer therapies on biodistribution and tumor function using specific radiopharmaceuticals.

Acknowledgment

This study is supported by a grant from the U. S. Department of Energy (Grant DOE DE-FG02–84ER-60218. The microPET imaging is supported by an NIH/NCI SAIRP grant (1 R24 CA83060). We would also like to thank the Small Animal Imaging Core of the Alvin J. Siteman Cancer Center at Washington University and Barnes-Jewish Hospital in St. Louis, Missouri for additional support of the microPET imaging. The Core is supported by an NCI Cancer Center Support (Grant 1 P30 CA91842). The authors wish to thank Margaret M. Morris and Mark A. Norte for their technical support, and Sally W. Schwarz for the production of isotopes. We also thank Jason S. Lewis, Yuan-Chuan Tai and Michelle E. Weber for helpful discussion as well as expertly editing the manuscript. A preliminary report of this work was presented at the 48th Annual Meeting of the Society of Nuclear Medicine in Toronto, Canada in 2001 [11].

References

[1] F. Dehdashti, J.E. Mortimer, B.A. Siegel, L.K. Griffeth, T.J. Bonasera, M.J. Fusselman, D.D. Detert, P.D. Cutler, J.A. Katzenellenbogen, M.J. Welch, Positron tomographic assessment of estrogen receptors in breast cancer: comparison with FDG-PET and in vitro receptor assays, J. Nucl. Med. 36 (1995) 1766–1774.

[2] A. Jemal, A. Thomas, T. Murray, M. Thun, Cancer statistics, CA Cancer J. Clin. 52 (2002) 23–47.

[3] K. Hamacher, H.H. Coenen, G. Stocklin, Efficient stereospecific synthesis of no-carrier-added 2-[18F]-fluoro-2-deoxy-D-glucose using aminopolyether supported nucleophilic substitution, J. Nucl. Med. 27 (1986) 235–238.

[4] C. Huggins, C.V. Hodges, Studies on prostate cancer: I. The effect of estrogen and of androgen injection on serum phosphatases in metastatic carcinoma of the prostate, Cancer Res. 1 (1941) 293–297.

[5] D.O. Kiesewetter, M.R. Kilbourn, S.W. Landvatter, D.F. Heiman, J.A. Katzenellenbogen, M.J. Welch, Preparation of tumor fluorine-18-labeled estrogens and their selective uptake in target tissues of immature rats, J. Nucl. Med. 25 (1984) 1212–1221.

[6] T. Kihlberg, S. Valind, B. Langstrom, Synthesis of [1-^{11}C], [2-^{11}C], [1-^{11}C]($^{2}H_3$) and [2-^{11}C]($^{2}H_3$) acetate for in vivo studies of myocardium using PET, Nucl. Med. Biol. 21 (1994) 1067–1072.

[7] H. Kishi, S. Minowada, N. Kosaka, H. Hara, 11C-choline PET helps determine the outcome of hormonal therapy of prostate cancer, J. Nucl. Med. 43 (2002) 117P.

[8] U.G. Mueller-Lisse, M.G. Swanson, D.B. Vigneron, H. Hricak, A. Bessette, R.G. Males, P.J. Wood, S. Noworolski, S.J. Kurhanewicz, Time-dependent effects of hormone-deprivation therapy on prostate metabolism as detected by combined magnetic resonance imaging and 3D magnetic resonance spectroscopic imaging, Magn. Reson. Med. 46 (2001) 49–57.

[9] N. Oyama, H. Akino, H. Kanamaru, Y. Suzuki, S. Muramoto, Y. Yonekura, N. Sadato, K. Yamamoto, K. Okada, ^{11}C-acetate PET imaging of prostate cancer, J. Nucl. Med. 43 (2002) 181–186.

[10] N. Oyama, H. Akino, Y. Suzuki, H. Kanamaru, H. Ishida, K. Tanase, N. Sadato, Y. Yonekura, K. Okada, FDG PET for evaluating the change of glucose metabolism in prostate cancer after androgen ablation, Nucl. Med. Commun. 22 (2001) 963–969.

[11] N. Oyama, L.A. Jones, T.L. Sharp, M.J. Welch, Androgenic control of glucose and acetate metabolism in rat prostate and prostate cancer tumor model, J. Nucl. Med. 42 (2001) 26P.

[12] T.A. Stamey, J.E. McNeal, C.M. Yemoto, B.M. Sigal, I.M. Johnstone, Biological determinants of cancer progression in men with prostate cancer, JAMA, 281 (1999) 1395–1400.

[13] E.K. Symes, Uptake and retention of androgens by the rat ventral prostate and consideration of their use as site directing agents, Biochem. Pharmacol. 31 (1982) 3231–3236.

[14] Y.C. Tai, A. Chatziioannou, S. Siegel, J. Young, D. Newport, R.N. Goble, R.E. Nutt, S.R. Cherry, Performance evaluation of the microPET P4: a PET system dedicated to animal imaging, Phys. Med. Biol. 46 (2001) 1845–1862.

[15] T. Yoshimoto, S. Waki, Y. Yonekura, N. Sadato, T. Murata, N. Omata, N. Takahashi, M.J. Welch, Y. Fujibayashi, Characterization of acetate metabolism in tumor cells in relation to cell proliferation: acetate metabolism in tumor cells, Nucl. Med. Biol. 28 (2001) 117–122.

DOTA–D-Tyr^1-Octreotate: A Somatostatin Analogue for Labeling with Metal and Halogen Radionuclides for Cancer Imaging and Therapy

Wen Ping Li,[†] Jason S. Lewis,[†] Joonyoung Kim,[†] Joseph E. Bugaj,[‡] Michael A. Johnson,[‡] Jack L. Erion,[‡] and Carolyn J. Anderson*,[†]

Mallinckrodt Institute of Radiology, Washington University School of Medicine, St. Louis, Missouri 63110 and Mallinckrodt, Inc. 675 McDonnell Blvd., St. Louis, Missouri 63134. Received December 10, 2001; Revised Manuscript Received April 25, 2002

The goal of this study was to evaluate a somatostatin receptor ligand, DOTA–D-Tyr^1-octreotate (DOTA-DY1-TATE), that has the chelator 1,4,7,10-tetraazacyclotetradecane-*N*,*N*′,*N*″,*N*‴-tetraacetic acid (DOTA) attached to the D-Tyr^1 residue, allowing radiolabeling with both radiohalogens and radiometals. A potential advantage of having a chelator attached to the Tyr^1 residue is that halogen radiolabels may residualize or remain trapped in tumor cells rather than clear from the tumor. DOTA-DY1-TATE was synthesized by solid-phase methods and radiolabeled with ^{61}Cu, ^{64}Cu, and ^{125}I in high radiochemical purity and specific activity. A competitive binding assay demonstrated that ^{nat}Cu-DOTA-DY1-TATE and DOTA-^{nat}I-DY1-TATE had comparable affinity to ^{nat}In-DTPA-OC in AR42J rat pancreatic tumor cells membranes. ^{61}Cu-DOTA-DY1-TATE had a dissociation constant (K_d) of 176.4 pM and a receptor concentration (B_{max}) of 244.4 fmol/mg. A tumor uptake of 1.515 %ID/g was determined for ^{64}Cu-DOTA-DY1-TATE and 0.814 %ID/g for DOTA-^{125}I-DY1-TATE in AR42J tumor bearing Lewis rats at 1 h postinjection. DOTA-^{125}I-DY1-TATE remained in the tumor at a higher concentration out to 4 h postinjection, suggesting that the iodine may have residualized in the tumor cells. MicroPET imaging of ^{64}Cu-DOTA-DY1-TATE in AR42J tumor bearing rats and SCID mice at 2 h postinjection showed significant uptake and good contrast in the thigh tumors in the rat model and in the neck and thigh tumors of the mouse. This study demonstrates that DOTA-DY1-TATE is a somatostatin analogue that can be labeled with both metal and halogen radionuclides, and its ^{64}Cu- and ^{125}I-radiolabeled compounds showed somatostatin receptor-mediated uptake in normal and tumor tissues.

INTRODUCTION

Over the last 15 years, considerable progress has been made in the investigation of radiolabeled somatostatin analogues as radiotherapeutic agents for somatostatin receptor-positive tumors. A number of studies have focused on improving the target tissue uptake of radiolabeled somatostatin analogues. It has been shown that changing the C-terminus from an alcohol to a carboxylic acid increases uptake of the peptide in somatostatin subtype 2 receptor (SSTR2)-positive tissues (*1*–*3*). It has further been shown that replacing the N-terminal D-Phe in octreotide with D-Tyr allows iodination of the N-terminus and subsequent residualization of the iodinated D-amino acid (*4*). Therefore, in this current study we synthesized DOTA–D-Tyr^1-octreotate (DOTA-DY1-TATE, Figure 1) to allow both radiolabeling with halogens (e.g., ^{124}I, ^{125}I, ^{131}I, ^{76}Br, ^{77}Br), as well as radiometals (e.g., ^{86}Y, ^{90}Y, ^{68}Ga, ^{177}Lu, ^{111}In, ^{64}Cu). One of our goals is to achieve higher somatostatin receptor binding affinity and better target tissue uptake as well as allow halogen radionuclides to residualize in target tissues.

The use of positron-emitting halogen radionuclides, specifically ^{124}I ($t_{1/2}$ = 4.2 d) and ^{76}Br ($t_{1/2}$ = 16 h), to label radiopharmaceuticals for PET imaging has increased greatly over the past decade. For example, ^{76}Br has been labeled to octreotide (*5*) and ^{76}Br-labeled bromodeoxyuridine has been investigated as a tumor and brain imaging agent (*6*, *7*). Iodine-124 is currently used to produce [^{124}I]-5-iodo-2′-fluoro-1-β-D-arabinofuranosyl-uracil (FIAU) which has been used to image gene expression (*8*). Copper-64 [$t_{1/2}$ = 12.8 h; 40% β^- (0.656 MeV); 19% β^+ (0.6 MeV); 38% EC] has diverse applications in radiopharmaceutical chemistry for PET imaging as well as therapy (*9*, *10*). Copper-61 [$t_{1/2}$ = 3.35 h; 60% β^+ (1.21 MeV); 40% EC] is another cyclotron-produced positron-emitting radionuclide that is made at Washington University using the same targetry system as is used for ^{64}Cu (*11*). Moreover, ^{61}Cu and ^{64}Cu can be produced on demand in high yield and in high specific activity on a small biomedical cyclotron (*11*, *12*).

The AR42J rat pancreatic carcinoma cell line is known to express SSTR2 both in vitro and in vivo (*13*, *14*). AR42J cells grown in culture were utilized to evaluate the in vitro binding affinity and were implanted in

* Corresponding author: Carolyn J. Anderson, Ph.D., Mallinckrodt Institute of Radiology, Washington University School of Medicine, 510 S. Kingshighway Blvd., Campus Box 8225, St. Louis, MO 63110. Phone: (314) 362-8427; fax: (314) 362-9940, e-mail: andersoncj@mir.wustl.edu.

[†] Washington University School of Medicine.

[‡] Mallinckrodt, Inc.

[1] Abbreviations used: DTPA, diethylenetriaminepentaacetic acid; DOTA, 1,4,7,10-tetraazacyclododecane-*N*,*N*′,*N*″,*N*‴-tetraacetic acid; TETA, 1,4,8,11-tetraazacyclotetradecane-*N*,*N*′,*N*″,*N*‴-tetraacetic acid; Y3, tyrosine-3; OC, octreotide; TATE, octreotate; D-Tyr^1, DY1; somatostatin subtype 2 receptor, SSTR2; positron emission tomography, PET; confidence interval, CI.; region of interest, ROI.

10.1021/bc015590k CCC: $22.00
Published on Web 05/25/2002

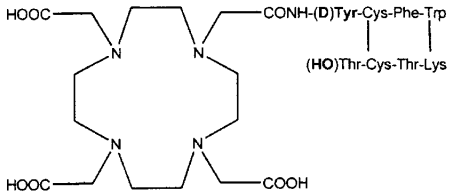

Figure 1. Structure of DOTA−D-Tyr^1-octreotate (DOTA-DY1-TATE).

immature, normal Lewis rats for in vivo biodistribution and microPET imaging. In this study, we determined the in vitro binding affinity of copper-labeled DOTA-DY1-TATE to AR42J tumor cell membranes and investigated the in vivo biodistribution of ^{64}Cu-DOTA-DY1-TATE and DOTA-^{125}I-DY1-TATE in AR42J tumor bearing rats. MicroPET imaging studies of ^{64}Cu-DOTA-DY1-TATE were carried out in the AR42J tumor-bearing SCID mice and immature Lewis rats.

MATERIALS AND METHODS

Materials and Analyses. ^{61}Cu and ^{64}Cu were produced on a Cyclotron Corporation CS-15 biomedical cyclotron at Washington University of School of Medicine, using previously reported methods (*11*, *12*). Sodium[^{125}I]-iodide was purchased from NEN LifeScience (Boston, MA). Indium-111-chloride ($^{111}InCl_3$) was obtained from Mallinckrodt, Inc. (St. Louis, MO). IODO-GEN precoated iodination tubes were purchased from Pierce (Rockford, IL). Reversed-phase extraction C-18 SepPak Light cartridges were obtained from Waters (Milford, MA). Ammonium acetate (NH_4OAc) was purchased from Fluka Chemical Co. (Ronkonkoma, NY); Copper acetate (99.99%) and indium acetate (99.95%) were purchased from Alfa Morton Thiokol Inc. (Danvers, MA). Trifluoroacetic acid (TFA) was obtained from J. T. Baker (Chicago, IL). All other chemicals were purchased from Aldrich Chemical Co., Inc. (Milwaukee, WI). All solutions were prepared using ultrapure water (18 MΩ-cm resistivity). Thin-layer chromatography (TLC) was performed using Whatman $MKC_{18}F$ reversed phase plates with 10% ammonium acetate:methanol (30:70) as the mobile phase. Radio-TLC detection was accomplished using a BIOSCAN System 200 Imaging Scanner (Washington, DC). Analytical reversed-phase HPLC was accomplished on a Waters (Milford, MA) 600E chromatography system with a Waters 991 photodiode array detector and an Ortec Model 661 (EG&G Instruments, Oak Ridge, TN) radioactive detector. Millenium 32 software (Waters, Milford, MA) was used to quantify chromatograms by integration. All HPLC samples were analyzed on a Vydac Protein & Peptide C-18 column (2.2 × 25 cm). The mobile phase was H_2O (0.1% TFA) (solvent A) and 90% acetonitrile (ACN) (0.1% TFA) (solvent B). The gradient consisted of 5% B to 75% B in 25 min (1.0 mL/min flow rate). Radioactive samples were counted using a Beckman 8000 automated well-type counter (Fullerton, CA).

Preweaned (21-day old, 40−50 g) male Lewis rats were purchased from Charles River Laboratories (Boston, MA) and Female SCID-Fox Chase CB-17 mice (29−35 days old, 25−30 g) were purchased from Taconic Farms Inc (Germantown, NY). The AR42J tumor line was obtained from American Type Culture Collection (ATCC, Rockville, MD).

Synthesis of DY1-TATE and DOTA-DY1-TATE. The synthesis of DYI-TATE and DOTA-DY1-TATE were accomplished by using similar methods previously described (*3*). Briefly, solid-phase peptide synthesis (SPPS) was carried out on an Applied Biosystems model 432A "Synergy" peptide synthesizer using the Fmoc (9-fluorenylmethoxy-carbonyl) methodology. Activated Fmoc-protected amino acids (25 μmol) were required by the instrument protocol. Activation was performed by combining 1-hydroxybenzotriazole (HOBt) and 2-(1*H*-benzotriazol-1-yl)-1,1,3,3-tetramethyluronium hexafluorophosphate (HBTU). DOTA-tris(*tert*-butyl ester) (Macrocyclics, Dallas, TX) was activated and coupled to Fmoc-protected amino acid. Final purifications of the peptides were accomplished by reversed-phase HPLC, employing a Vydac Protein & Peptide C-18 column (2.2 × 25 cm).

Preparation of Radiolabeled Somatostatin Analogues. DTPA-OC was labeled with ^{111}In as previously described (*15*). Radiolabeling with ^{61}Cu and ^{64}Cu was carried out by addition of 1−5 mCi (37−185 MBq) of ^{61}Cu or ^{64}Cu in 0.1 M ammonium acetate (pH 6.5) to 1−5 μg of the peptide in 0.1 M ammonium acetate followed by 30 min incubation at 65 °C as previously reported (*16*). The $^{64/61}$Cu-labeled DOTA-DY1-TATE was purified on a C-18 SepPak Light cartridge, using 100% ethanol as the elution solvent, and radiochemical purity was determined by radio-TLC or radio-HPLC.

Radioiodinated DOTA-DY1-TATE was synthesized using the IODO-GEN method (*17*, *18*). Briefly, Na[^{125}I] [300−400 μCi (11.1−14.8 MBq)] was added to 10 μg of DOTA-DY1-TATE diluted with 0.01 M PBS (100 μL) in a glass vial coated with IODO-GEN (50 μg). The reaction mixture was removed from the reaction vessel following 25 min of incubation at room temperature. The solution was then diluted with 3 mL of water. The resulting solution was eluted through a C-18 reversed-phase extraction cartridge, which was preconditioned with 5 mL of 70% ethanol and subsequently activated with 5 mL of 2-propanol. The cartridge was rinsed successively with 5 mL of distilled water and 5 mL of 0.5 M acetic acid. The radioiodinated peptide was eluted in 5 mL of 96% ethanol, and the solvent was evaporated at room temperature under a gentle stream of nitrogen. The dry residue was reconstituted in 1−3 mL of 0.9% NaCl.

The cold copper and indium agents (^{nat}Cu-DOTA-DY1-TATE, ^{nat}Cu-DOTA-Y3-TATE, ^{nat}In-DTPA-OC) for the receptor binding assays were prepared by the reaction of copper and indium acetate using the same procedure described above for radiolabeling of DOTA-DY1-TATE with ^{61}Cu, ^{64}Cu, and ^{111}In. DOTA-^{nat}I-DY1-TATE was synthesized by following the same procedure as for DOTA-^{125}I-DY1-TATE, and the reaction yield was confirmed by HPLC.

In Vitro Receptor Binding Assay. The binding affinity of Cu-DOTA-DY1-TATE was measured in AR42J rat pancreatic tumor membranes using methods previously described with minor modifications (*9*). Briefly, ^{61}Cu-DOTA-DY1-TATE was displaced with increasing concentrations of ^{nat}Cu-DOTA-DY1-TATE. A competitive binding assay was performed by displacing ^{111}In-DTPA-OC with the competing ligands ^{nat}Cu-DOTA-DY1-TATE, ^{nat}Cu-DOTA-Y3-TATE, ^{nat}In-DTPA-OC and DOTA-^{nat}I-DY1-TATE. Assays were carried out using the Millipore Multiscreen system (Bedford, MA) (*9*). The best-fit IC_{50} values, the dissociation constant (K_d), and the number of SSTR2 binding sites (B_{max}) for the AR42J cells were calculated using PRISM (Graphpad, San Diego, CA).

Animal Models. All animal experiments were performed in compliance with the Guidelines for the Care and Use of Research Animals established by Washington

University's Animal Studies Committee. For AR42J tumor-bearing mice, AR42J cells were grown as xenografts in female SCID mice. Briefly, AR42J cells (1×10^7), grown in F-12K Nutrient mixture medium containing 20% fetal calf serum (FCS) were injected subcutaneously, bilaterally, into flanks and necks of female SCID mice (*19*). The tumors were allowed to grow 10−12 days until 0.5−0.9 g in size. Male Lewis rats (21 d old) were implanted with AR42J tumors in the necks or/and left legs from tumor obtained from Mallinckrodt, Inc (St. Louis, MO) (passage 36) and maintained by serial passage in animals. Tumor was excised from euthanized rats and was rinsed with sterile saline and placed on ice in a Petri dish containing Gibco Media 199 (Sigma Chemical Co., St. Louis, MO). Connective and necrotic tissue were removed, and the material was diced into small pieces (2×2 mm). The freshly dissected pieces were delivered to the left flank of the animal via a 13-gauge trocar inserted subcutaneously. AR42J tumor growth was observed for 2 weeks after implantation, and tumors achieved a solid, palpable mass of 1.0−1.5 g in size by ~14 days postimplantation.

Biodistribution of ^{64}Cu-DOTA-DY1-TATE and DOTA-^{125}I-DY1-TATE. Biodistribution studies were carried out using immature (~33 day old) male Lewis rats bearing AR42J tumors (12 days post-implant) in the left flank. Anesthetized animals received a coinjection of ^{64}Cu-DOTA-DY1-TATE and DOTA-^{125}I-DY1-TATE (32 μCi for ^{64}Cu, 5 μCi for ^{125}I, 0.68 μg peptide for each compound) via the tail vein. The animals were euthanized at 1, 4, 24, and 72 h postinjection. A group of 5 rats were coinjected with a blocking dose of DY1-TATE (150 μg) and sacrificed 1 h postinjection. Following euthanization, the tissues and organs of interest were removed and weighed, and the radioactivity was measured in a gamma counter. Standards (n = 5) were prepared to verify the counting efficiency of the gamma counter for each radionuclide. Samples were first counted for ^{64}Cu using a specific energy window that did not have detectable crossover for ^{125}I. After allowing for complete decay of the ^{64}Cu (>12 half-lives), the samples were then counted using the energy window specific for ^{125}I. The percent injected dose per gram (% ID/g) and percent injected dose per organ (% ID/organ) were calculated by comparison with standards representing the injected dose per animal. A group of five rats that were sacrificed at 72 h postinjection were housed in individual metabolism cages for the collection of urine and feces at various time points from 1 to 72 h for determination of the %ID excreted.

MicroPET Images. Positron emission tomography (PET) imaging was performed on the first commercially available microPET (Concorde Microsystems, Knoxville, TN) which was based on the design of Cherry and colleagues (*20*). Imaging studies were carried out on four SCID mice and four male Lewis rats carrying AR42J tumors. Two mice bearing tumors on the neck and left leg and four rats (two rats had tumors on neck and left leg, the other two rats had tumors on left legs only) were imaged on the microPET at selected times postinjection. Two tumor-bearing mice were each injected with 1 mCi ^{64}Cu-DOTA-DY1-TATE (1 mCi/μg for control, 1 mCi/50 μg for blocked) and imaged at 10 min, 1, 2, and 4 h postinjection. The two mice were imaged side by side and remained in the same bed position for all time points. Four rats were each injected with 2.5 mCi ^{64}Cu-DOTA-DY1-TATE (2.5 mCi/μg for control, 2.5 mCi/150 μg for blocked) and imaged at 10 min, 1, 2, and 4 h. Each rat was imaged in two bed positions. Immediately after imaging, the %ID/g of tumor from the rats was determined by measuring the dissected tumors in a dose calibrator (Capintec, Ramsey, NJ). Tumor, kidney, and liver activities of ^{64}Cu were generated by measuring regions of interest (ROIs) that encompassed the entire organ from the microPET images in AR42J tumor-bearing SCID mice and Lewis rats after 2 and 4 h postinjection.

Statistical Methods. To compare differences between the data, a student's t-test was performed using Prism (Graphpad, San Diego, CA). Differences at the 95% confidence level ($p < 0.05$) were considered significant.

RESULTS

Chemistry and Radiochemistry. The DY1-TATE and DOTA-DY1-TATE were analyzed by analytical reversed-phase HPLC (UV detection 214 nm) using conditions described in the Methods section and by LC-MS. DY1-TATE: HPLC retention time = 17.9 min; MS, *m/z* calculated for $C_{49}H_{64}N_{10}O_{12}S_2$ $(M + H)^+ = 1048.4$, found 1049.3. DOTA-DY1-TATE: HPLC retention time = 20.4 min; MS, *m/z* calculated for $C_{65}H_{90}N_{14}O_{19}S_2$ $(M + H)^+ = 1434.7$, found 1435.6. ^{111}In-DTPA-OC and $^{61/64}$Cu-DOTA-DY1-TATE were prepared in ≥98% radiochemical purity. Specific activities for both ^{111}In- and $^{61/64}$Cu-labeled conjugates ranged from 1500 to 3500 Ci/mmol (56000 to 111000 GBq/mmol). The radiochemical purity of DOTA-^{125}I-DY1-TATE was confirmed to be greater than 98% by radio-HPLC. DOTA-DY1-TATE was typically labeled with ^{125}I to a specific activity of 300 Ci/mmol (11000 GBq/mmol). The reaction yields for "cold" somatostatin analogues were greater than 98% as confirmed by radio-TLC of an exchange reaction between natural Cu^{2-} or In^{3-} with ^{64}Cu or ^{111}In, respectively.

In Vitro Receptor Binding Assay. A homogeneous competitive binding assay was performed using AR42J tumor membranes, where ^{61}Cu-DOTA-DY1-TATE was challenged with increasing concentrations of ^{nat}Cu-DOTA-DY1-TATE. The IC_{50} value for ^{nat}Cu-DOTA-DY1-TATE was determined to be 1.35 nM, with a 95% confidence interval (CI) of 1.02 to 1.8 nM (Figure 2A). Scatchard analysis of the data showed a K_d of 176.4 pM (95% CI 158.4 to 201.3 pM) and a somatostatin B_{max} in the AR42J membranes of 244.4 fmol/mg (95% CI 219.7 to 274.1 fmol/mg) of membrane protein (Figure 2B).

A competitive binding assay was performed between four somatostatin analogues vs ^{111}In-DTPA-OC. The concentration of the radioligand in the binding assays was 0.05 nM. The IC_{50} values were 1.78 nM for Cu-DOTA-Y3-TATE, 4.62 nM for Cu-DOTA-DY1-TATE, 4.8 nM for DOTA-I-DY1-TATE, and 4.87 nM for In-DTPA-OC (Figure 3 and Table 1). These results suggest that Cu-DOTA-DY1-TATE and DOTA-I-DY1-TATE have similar binding affinity to AR42J cells as In-DTPA-OC, while the analogue with Tyr in the 3-position has somewhat higher binding affinity.

Biodistribution Studies. Summaries of the biodistribution data are shown in Figure 4. Rapid clearance of the radioactivity from the blood circulation was observed for both compounds. At all times of analysis the average uptake of ^{64}Cu activity in tumors was approximately twice as high as ^{125}I activity ($p < 0.03$). The highest tumor uptake of ^{64}Cu-DOTA-DY1-TATE (1.515 ± 0.154 %ID/g) was found after 1 h postinjection, and was 1.247 ± 0.250 %ID/g at 4 h postinjection, suggesting that the ^{64}Cu was residualized in the tumor out to at least 4 h postinjection. A similar trend was observed for DOTA-^{125}I-DY1-TATE (0.814 ± 0.058%ID/g at 1 h, 0.543 ± 0.016

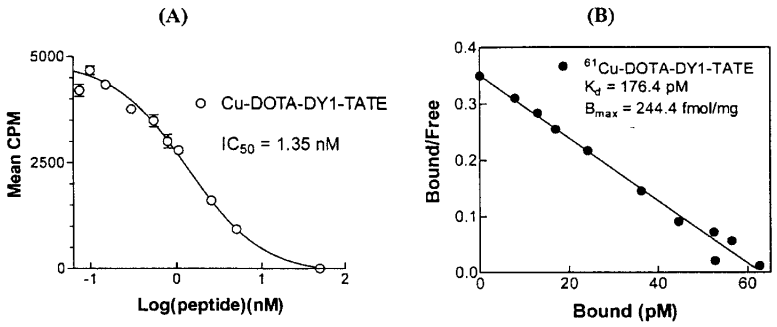

Figure 2. The in vitro binding affinity of ^{61}Cu-DOTA-DY1-TATE to AR42J rat pancreatic tumor membranes blocked with increasing concentrations of unlabeled Cu-DOTA-DY1-TATE (n = 6 for each data point).

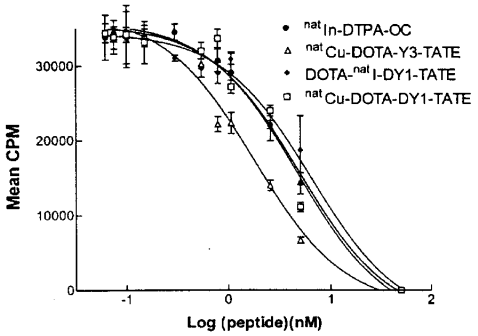

Figure 3. Competitive binding assay of Cu-DOTA-DY1-TATE, DOTA-I-DY1-TATE, Cu-DOTA-Y3-TATE, and In-DTPA-OC displacing ^{111}In-DTPA-OC in AR42J tumor membranes (n = 3 for each data point).

Table 1. IC_{50} Values for Competitive Binding Assay of ^{nat}Cu-DOTA-DY1-TATE, DOTA-^{nat}I-DY1-TATE, ^{nat}Cu-DOTA-Y3-TATE, and ^{nat}In-DTPA-OC Displacing ^{111}In-DTPA-OC in AR42J Tumor Membranes (n = 3 for each data point)

competing ligand	IC_{50} (nM)	95% CI (nM)
^{nat}Cu-DOTA-Y3-TATE	1.78	1.29–2.46
^{nat}Cu-DOTA-DY1-TATE	4.62	3.28–6.52
DOTA-^{nat}I-DY1-TATE	4.58	3.13–6.69
^{nat}In-DTPA-OC	4.87	3.98–5.96

%ID/g at 4 h) in the tumors. In the rats that received the co-injected blocking dose, the uptake in the tumor of ^{64}Cu-DOTA-DY1-TATE (0.468 ± 0.046 %ID/g) and DOTA-^{125}I-DY1-TATE (0.323 ± 0.016 %ID/g) was significantly lower at 1 h postinjection (p < 0.02) (Table 2). The higher uptake of ^{64}Cu-labeled conjugate in the tumor compared to ^{125}I-labeled conjugate may be due to a greater degree of retention of ^{64}Cu-DOTA-DY1-TATE in the tumor compared to DOTA-^{125}I-DY1-TATE. Since time points earlier than 1 h were not evaluated for the biodistribution studies, it is difficult to know whether the uptake of DOTA-^{125}I-DY1-TATE in the tumor peaked prior to 1 h.

The uptake in the pituitary and the pancreas at 1 h postinjection was significantly higher with ^{64}Cu-DOTA-DY1-TATE (1.985 ± 0.334 %ID/g for pituitary, 1.490 ± 0.337 %ID/g for pancreas) compared with DOTA-^{125}I-DY1-TATE (1.246 ± 0.160 %ID/g for pituitary, 0.850 ± 0.203 %ID/g for pancreas) (p < 0.05). Uptake in the SSTR2-rich pituitary, adrenals, and pancreas was blocked with unlabeled DY1-TATE for both the ^{125}I and ^{64}Cu-labeled peptides, suggesting receptor-mediated uptake of both compounds in these tissues (Table 2). No appreciable differences were observed for non-somatostatin-receptor-positive tissues between rats that received a coinjection of blocking dose and unblocked rats.

Liver uptake for DOTA-^{125}I-DY1-TATE at all times of analysis was lower than for ^{64}Cu-DOTA-DY1-TATE. However, the kidney uptake of DOTA-^{125}I-DY1-TATE (9.761 ± 1.036 %ID/g at 1 h, 9.450 ± 0.255 %ID/g at 4 h, 8.190 ± 0.646 %ID/g at 24 h, 5.921 ± 0.880 %ID/g at 72 h) was 3-fold higher than that of ^{64}Cu-DOTA-DY1-TATE (2.888 ± 0.187 %ID/g at 1 h, 2.389 ± 0.202 %ID/g at 4 h, 1.740 ± 0.061 %ID/g at 24 h, 1.206 ± 0.158 %ID/g at 72 h). The kidney clearance of DOTA-^{125}I-DY1-TATE maintained a level of 5.921 ± 0.880 %ID/g even after 72 h postinjection. This high kidney uptake and longer retention time of DOTA-^{125}I-DY1-TATE was similar to that of ^{125}I-DY1-TATE and DTPA-^{125}I-DY1-TATE (*4*). This is most likely due to the longer residence time of the DOTA-^{125}I-DY1 residue in the kidneys compared to ^{125}I-L-amino acids. Except for ^{125}I activity in thyroid, normal tissue uptake of DOTA-^{125}I-DY1-TATE decreased throughout the period.

The highest tumor:blood ratios were found at 4 h postinjection for both ^{64}Cu- and ^{125}I-labeled DOTA-DY1-TATE in AR42J tumor-bearing Lewis rats (7.8 ± 1.5 and 8.8 ± 0.9, respectively). For DOTA-^{125}I-DY1-TATE, the tumor-to-blood ratio maintained at high levels out to 24 h postinjection (6.4 ± 1.0), while for ^{64}Cu-DOTA-DY1-TATE the ratio dropped to 2.6 ± 0.6. Tumor:muscle ratios were similar for ^{64}Cu- and ^{125}I-labeled DOTA-DY1-TATE, with the peak ratio occurring at 4 h (19.2 ± 3.8 and 21.9 ± 2.5, respectively).

The excretion data demonstrated that 59.18 ± 21.05 %ID for ^{64}Cu and 64.22 ± 19.93 %ID for ^{125}I was excreted from the urine by 4 h postinjection. By 24 h postinjection, ~75 %ID of ^{64}Cu-DOTA-DY1-TATE activity was found in the urine and feces, and ~85 %ID of DOTA-^{125}I-DY1-TATE activity was excreted (Table 3).

MicroPET Images. Figure 5A shows the coronal microPET images of AR42J tumor-bearing SCID mice, 2 h postadministration of ^{64}Cu-DOTA-DY1-TATE, with and without a coinjected blocking dose of DY1-TATE. Uptake in the neck and thigh tumors was visible at 2 h postinjection for the control mouse (left). Conversely, the other mouse (right) that received a blocking dose showed reduced uptake at both tumor sites. Prominent uptake was observed in the liver and kidneys in both animals.

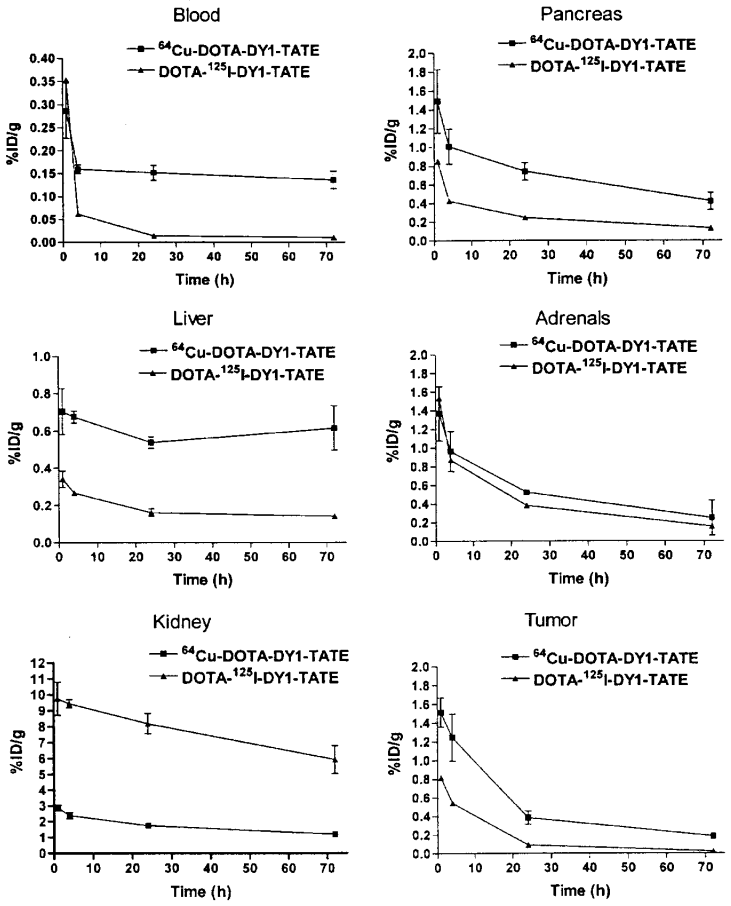

Figure 4. Biodistribution data of ^{64}Cu-DOTA-DY1-TATE and DOTA-^{125}I-DY1-TATE in normal and SSTR2 positive tissues (blood, liver and kidneys, pancreas, adrenals, tumor). Data are presented as %ID/g ± SD, $n = 5$ for each time point.

Table 2. Biodistribution of ^{64}Cu-DOTA-DY1-TATE and DOTA-^{125}I-DY1-TATE in AR42J Tumor Bearing Lewis Rats at 1 h, with and without a Coadministration of Blocking Agent[a]

tissue	^{64}Cu, 1 h	^{64}Cu, 1 h block	^{125}I, 1 h	^{125}I, 1 h block
blood	0.287 ± 0.060	0.361 ± 0.065	0.354 ± 0.073	0.434 ± 0.064
liver	0.705 ± 0.122	0.981 ± 0.199	0.342 ± 0.045	0.352 ± 0.036
kidney	2.888 ± 0.187	3.626 ± 0.176	9.761 ± 1.036	10.895 ± 0.863
pituitary	1.985 ± 0.334	0.516 ± 0.456	1.246 ± 0.160	0.325 ± 0.208
adrenals	1.369 ± 0.291	0.234 ± 0.066	1.534 ± 0.351	0.212 ± 0.036
pancreas	1.490 ± 0.337	0.409 ± 0.059	0.850 ± 0.203	0.270 ± 0.024
tumor	1.515 ± 0.154	0.468 ± 0.046	0.814 ± 0.058	0.323 ± 0.016
thyroid	0.307 ± 0.040	0.388 ± 0.083	1.357 ± 0.131	1.234 ± 0.023

[a] Data are presented as % ID/g ± SD ($n = 5$).

Four hours after administration of ^{64}Cu-DOTA-DY1-TATE, both tumor sites in the nonblocked animal could still be easily identified, as well as showing higher uptake than other normal organs.

Figure 5B shows the microPET images in Lewis rats bearing AR42J tumors of ^{64}Cu-DOTA-DY1-TATE obtained after 2 h postinjection with and without the addition of DY1-TATE as a blocking agent. Imaging was performed at 1, 2, and 4 h postinjection. Similar to the AR42J tumor-bearing mice images, tumor uptake was also observed in the tumor-bearing rats. The most prominent region of ^{64}Cu-DOTA-DY1-TATE uptake was the bladder, due to the rapid excretion of this compound into the urine. In addition, significant uptake in the SSTR2-rich pituitary was observed.

Uptake of radioactivity in the tumor, kidney, and liver measured from the microPET images in the AR42J tumor-bearing SCID mice and Lewis rats after 2 and 4

Table 3. Excretion of ^{64}Cu-DOTA-DY1-TATE and DOTA-^{125}I-DY1-TATE in AR42J Tumor-Bearing Lewis Rats[a]

	^{64}Cu-DOTA-DY1-TATE			DOTA-^{125}I-DY1-TATE		
	4 h	24 h	48 h	4 h	24 h	48 h
urine	59.18 ± 21.05	65.36 ± 19.88	66.29 ± 20.35	64.22 ± 19.93	74.93 ± 21.77	77.76 ± 20.34
feces	<0.1	9.08 ± 9.45	11.12 ± 9.87	<0.1	9.79 ± 8.97	12.39 ± 5.42

[a] All data are reported as % ID ± SD (n = 5).

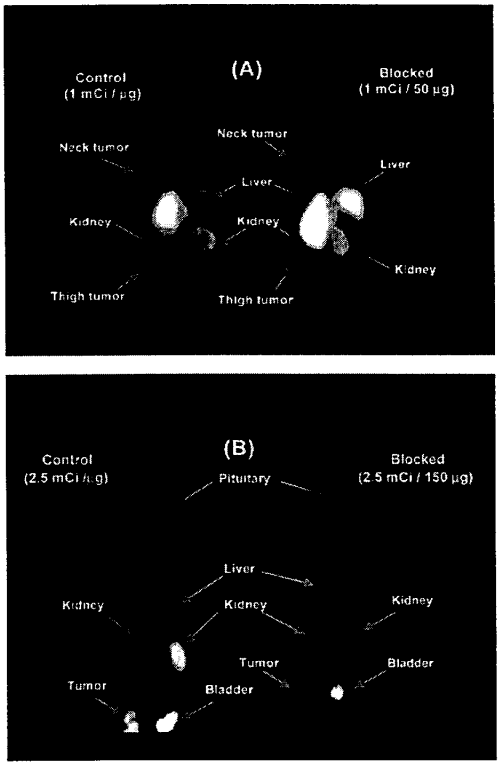

Figure 5. (A) Coronal microPET images of AR42J tumor-bearing SCID mice after 2 h postadministration of ^{64}Cu-DOTA-DY1-TATE, with and without a coinjected blocking dose (2.5 mCi/µg, left; 2.5 mCi/µg coinjected with 50 µg of DY1-TATE, right). (B) Coronal microPET images of AR42J tumor-bearing Lewis rats (2 bed positions) after 2 h postadministration of ^{64}Cu-DOTA-DY1-TATE, with and without a coinjected blocking dose (2.5 mCi/µg, left; 2.5 mCi/µg coinjected with 150 µg of DY1-TATE, right).

h postinjection are given in Figures 6A and 6B. In the SCID mice, the results suggested tumor activity in the control mice (0.02 µCi/µL at 2 h pi, 0.02 µCi/µL at 4 h pi) was about 2-fold higher than in blocked mice (0.01 µCi/µL for 2 h pi, 0.01 µCi/µL for 4 h pi). In SCID mice, the tumor activity was similar at both 2 and 4 h postinjection. In the 'blocked' Lewis rats, a similar reduction in activity was observed compared to control Lewis rats. Tumor activity in the control rats (0.03 µCi/µL for 2 h pi, 0.02 µCi/µL for 4 h pi) was 2−3-fold higher than in 'blocked' rats (0.01 µCi/µL for 2 h pi, 0.01 µCi/µL for 4 h pi). These results agreed with tumor uptake measurements that were determined by measuring the activity of the dissected tumor in a dose calibrator, where 4.14 ± 0.01 %ID/g was found in the control tumor and 1.46 ± 0.00 %ID/g was in the tumor of the rat coinjected with blocking agent. These data confirmed that tumor uptake was blocked with an excess of DY1-TATE. Moreover, blocking of tumor activity in the rats appeared to be more effective than in mice, which probably reflects the crossover activity from liver/kidney in mice that obscures the tumor, especially in the blocked mice when measuring regions of interest (ROIs) that encompassed the entire organ.

DISCUSSION

The utility of radiolabeled somatostatin analogues for imaging and therapy of cancer is well described in the literature. The majority of newly developed somatostatin analogues were specifically designed for labeling radiometals (*1*−*3*). The goal of this research was to design a somatostatin analogue for labeling both radiometals and halogens, with the added feature of having the halogen residualized in target tissue. Here we investigated DOTA-DY1-TATE, where the *C*-terminal alcohol of octreotide was replaced with a *C*-terminal acid (TATE). This analogue was labeled with ^{64}Cu and ^{125}I and compared in in vitro receptor binding assays and in vivo somatostatin-receptor-positive tumor-bearing animal models. Having a somatostatin analogue that allows the ability for labeling both metals and halogens will allow direct comparisons of these analogues with the only modification being the radionuclide used for labeling.

Receptor binding experiments using AR42J rat pancreatic tumor membranes were performed to verify the IC_{50} values of the new somatostatin analogues compared to ^{111}In-DTPA-OC. Scatchard analysis was performed with $^{61/nat}$Cu-DOTA-DY1-TATE to determine the K_d of this analogue. The unlabeled iodinated and copper complexed DOTA-DY1-TATE analogues had binding affinity that were comparable to In-DTPA-OC while the IC_{50} for Cu-DOTA-Y3-TATE was about 2−3-fold lower. These data are encouraging, since it demonstrates that the binding affinity was not compromised with the DY1-TATE analogues compared to the DTPA-OC and DOTA-Y3-TATE analogues. Another DY1 analogue (DTPA-^{125}I-DY1−OC) was described by Breeman et al. (*4*); however, this analogue had an IC_{50} value vs ^{125}I-Y3-OC that was 200-fold higher than ^{125}I-Y3-OC itself.

The biodistribution of ^{64}Cu- and ^{125}I-labeled DOTA-DY1-TATE were performed in one coinjection experiment in AR42J tumor-bearing Lewis rats. This model has several advantages compared to the typically utilized animal models, AR42J tumor-bearing nude/SCID mice, and CA20948-tumor bearing rats. AR42J cells grow both in cell culture and in animal models, which allows the advantage of comparing in vitro receptor binding studies and tumor-bearing animal studies using the same tumor cell line. The use of young rats (21 d) also allows the AR42J tumor cells to be implanted into immunocompetent rodents, rather than immunocompromised nude or SCID mice.

Greater somatostatin-receptor-mediated uptake was observed with ^{64}Cu-DOTA-DY1-TATE than DOTA-^{125}I-DY1-TATE in the pancreas as well as the AR42J tumor (p < 0.02), whereas the uptake was similar in the

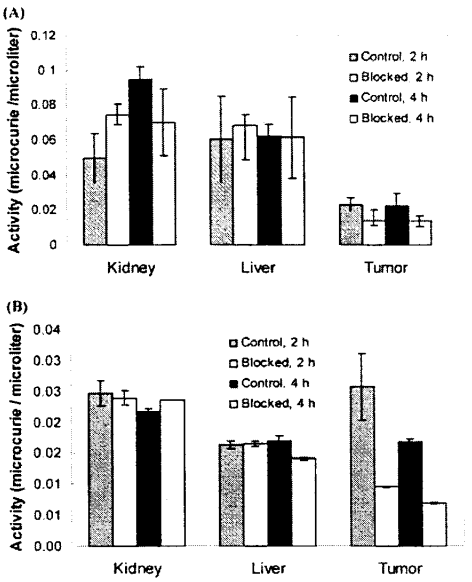

Figure 6. Tumor, kidney, and liver activity of ^{64}Cu after 2 and 4 h postadministration of ^{64}Cu-DOTA-DY1-TATE generated by measuring ROIs from microPET images in control and blocked AR42J tumor-bearing SCID mice (A) and Lewis rats (B). Each bar presents two animals.

adrenals. However, the liver and blood uptake of ^{64}Cu-DOTA-DY1-TATE were significantly greater than for DOTA-^{125}I-DY1-TATE ($p < 0.01$). The high uptake in the blood at longer time points and the increasingly high uptake in the liver was problematic for ^{64}Cu-DOTA-DY1-TATE, suggesting that ^{64}Cu dissociated from the DOTA chelator (*21*). Research is ongoing to develop more stable chelators for copper radionuclides that have greater kinetic stability, and these will eventually be conjugated to somatostatin analogues (*22*). It is predicted that conjugating a chelator to DY1-TATE that forms a more stable Cu(II) complex than DOTA will significantly decrease accumulation in the blood, liver and kidneys.

The uptake of ^{64}Cu- and ^{125}I-labeled DOTA-DY1-TATE was not as high in somatostatin-receptor positive tissues as has been observed for other radiolabeled somatostatin analogues. Comparisons between the AR42J tumor-bearing rat model can only be made with CA20948 tumor-bearing rats, since to the best of our knowledge, uptake of radiolabeled somatostatin analogues has not yet been reported for the AR42J tumor-bearing rat model. Therefore, comparisons with other somatostatin-receptor positive tissues are presented here. For example, the uptake of ^{64}Cu-TETA-Y3-TATE in the rat pancreas was 9.35 ± 1.66 %ID/g in Lewis rats (*19*) at 1 h postinjection, compared to 1.49 ± 0.34 %ID/g for ^{64}Cu-DOTA-DY1-TATE and 0.85 ± 0.20 %ID/g for DOTA-^{125}I-DY1-TATE. A biodistribution study of ^{177}Lu-DOTA-Y3-TATE in Lewis rats showed a pancreas uptake of 10.49 ± 1.91 %ID/g (*23*). However, the uptake of the DOTA-DY1-TATE analogues in the pancreas was comparable or greater than ^{64}Cu-TETA-OC (0.86 ± 0.14 %ID/g) and ^{111}In-DTPA-OC (0.42 ± 0.09 %ID/g) (*15*). Compared to DTPA-^{125}I-DY1−OC (*4*), the pancreas and adrenal uptakes of DOTA-^{125}I-DY1-TATE were somewhat higher (pancreas: 0.85 vs ~0.5 %ID/g, respectively; adrenal: 1.5 vs ~1.0 %ID/g, respectively). This suggests that the octreotate analogues may be superior to the octreotide analogues, which has been previously been reported (*2*, *3*).

Although the radiometal-labeled DOTA/TETA-Y3-TATE analogues showed superior receptor-mediated uptake, these analogues do not allow the ability to label via a residualizing label with radiohalogens. Therefore, the use of the DY1 analogues opens possibilities for the radiotherapeutic application of radioiohalogened ligands in patients with somatostatin receptor-positive tumors.

MicroPET imaging of ^{64}Cu-DOTA-DY1-TATE in AR42J tumor-bearing mice and rats at 2 h postinjection showed higher amounts of activity in the liver and kidneys compared to other normal tissues (Figure 6). The tumor also had significant uptake and showed good contrast compared with receptor-negative background tissue in the neck and thigh tumors of the mouse, and the thigh tumors in the rat model. In the AR42J-tumor bearing Lewis rats, the somatostatin receptor-positive pituitary was visualized, whereas it was not visualized in the rat coinjected with a blocking dose. Quantification of the activity in the rat tumor, liver, and kidney was comparable to the relative amounts determined by traditional biodistribution. The quantification of the microPET images also demonstrated that the activity in the tumor was significantly blocked, and this decrease in uptake corresponded to the visual decrease in uptake delineated in the images. These data suggest that microPET may be used as an alternative to traditional multiple animal biodistribution studies for screening new positron-emitting radiopharmaceuticals.

CONCLUSIONS

The study presented here demonstrates that DOTA-DY1-TATE is a peptide that can be labeled with both metal and halogen radionuclides. The IC_{50} values for ^{64}Cu- and ^{125}I-labeled DOTA-DY1-TATE were comparable to ^{111}In-DPTA-OC, and these analogues showed somatostatin receptor-mediated uptake in normal and tumor tissues in vivo. DOTA-^{125}I-DY1-TATE appeared to remain in the tumor out to 4 h postinjection, suggesting that the iodine was possibly residualized in the tumor cells. Future studies include microPET imaging in the AR42J tumor-bearing rat model with DOTA-DY1-TATE labeled with other positron-emitting radionuclides such as ^{76}Br, ^{124}I, and ^{86}Y.

ACKNOWLEDGMENT

The authors wish to thank Lynne Jones, Nicole Mercer, Mu Wang, Virginia Richey, and John Engelbach for technical assistance, and W. Barry Edwards, Ph.D. (MetaPhore Pharmaceuticals) for helpful discussions. This research was supported by NIH Grant R01 CA64475 (C.J.A.). The production of copper radionuclides at Washington University is supported by a grant from the National Cancer Institute (R24 CA86307 − M. J. Welch, P. I.). MicroPET imaging is supported by NIH/NCI SAIRP grant (1R24 CA83060). We would also like to thank the Small Animal Imaging Core of the Alvin J. Siteman Cancer Center at Washington University and Barnes Jewish Hospital in St. Louis, MO for additional support of the microPET imaging. The core is supported by a NCI Cancer Center Support Grant (1P30 CA91842).

LITERATURE CITED

(1) de Jong, M., Bakker, W. H., Breeman, W. A. P., Bernard, B. F., Hofland, L. J., Visser, T. J., Srinivasan, A., Schmidt, M., Behe, M., Maecke, H., and Krenning, E. P. (1998) Pre-

Clinical Comparison of [DTPA⁰]Octreotide, [DTPA⁰Tyr³]-Octreotide and [DOTA⁰Tyr³]Octreotide as Carriers for Somatostatin Receptor-Targeted Scintigraphy and Radionuclide Therapy. *Int. J. Cancer 75*, 406−411.

(2) de Jong, M., Breeman, W. A. P., Bakker, W. H., Kooij, P. P. M., Bernard, B. F., Hofland, L. J., Visser, T. J., Srinivasan, A., Schmidt, M., Erion, J. L., Bugaj, J. E., Maecke, H. R., and Krenning, E. P. (1998) Comparison of ^{111}In-Labeled Somatostatin Analogues for Tumor Scintigraphy and Radionuclide Therapy. *Cancer Res. 58*, 437−441.

(3) Lewis, J. S., Lewis, M. R., Srinivasan, A., Schmidt, M. A., Wang, J., and Anderson, C. J. (1999) Comparison of Four ^{64}Cu-labeled Somatostatin Analogues in vitro and in a Tumor-bearing Rat Model: Evaluation of New Derivatives for PET Imaging and Targeted Radiotherapy. *J. Med. Chem. 42*, 1341−1347.

(4) Breeman, W. A. P., de Jong, M., Bernard, B., Hofland, L. J., Srinivasan, A., Vanderpluijm, M., Bakker, W. H., Visser, T. J., and Krenning, E. P. (1998) Tissue Distribution and Metabolism of Radioiodinated DTPA(0), D.-Tyr(1) and Tyr-(3) Derivatives of Octreotide in Rats. *Anticancer Res. 18(1A)*, 83−89.

(5) Yngve, U., Khan, T. S., Bergstrom, M., and Langstrom, B. (2001) Labeling of Octreotide using Br-76-prosthetic Groups. *J. Lab. Compd. Radiopharm. 44*, 561−573.

(6) Gardelle, O., Roelcke, U., Vontobel, P., Crompton, N. E. A., Guenther, I., Blauenstein, P., Schubiger, P. A., Blattmann, H., Ryser, J. E., Leenders, K. L., and Kaser-Hotz, B. (2001) [Br-76]bromodeoxyuridine PET in Tumor-bearing Animals. *Nucl. Med. Biol. 28*, 51−57.

(7) Ryser, J. E., Blauenstein, P., Remy, N., Weinreich, R., Hasler, P. H., Novak-Hofer, I., and Schubiger, P. A. (1999) [Br-76]bromodeoxyuridine, a Potential Tracer for the Measurement of Cell Proliferation by Positron Emission Tomography, in vitro and in vivo Studies in Mice. *Nucl. Med. Biol. 26*, 673−679.

(8) Bennett, J. J., Tjuvajev, J., Johnson, P., Doubrovin, M., Akhurst, T., Malholtra, S., Hackman, T., Balatoni, J., Finn, R., Larson, S. M., Federoff, H., Blasberg, R., and Fong, Y. M. (2001) Positron Emission Tomography Imaging for Herpes Virus Infection: Implications for Oncolytic Viral Treatments of Cancer. *Nat. Med. 7*, 861−865.

(9) Anderson, C. J., Jones, L. A., Bass, L. A., Sherman, E. L. C., McCarthy, D. W., Cutler, P. D., Lanahan, M. V., Cristel, M. E., Lewis, J. S., and Schwarz, S. W. (1998) Radiotherapy, Toxicity and Dosimetry of Copper-64-TETA-Octreotide in Tumor-Bearing Rats. *J. Nucl. Med. 39*, 1944−1951.

(10) Anderson, C. J., Dehdashti, F., Cutler, P. D., Schwarz, S. W., Laforest, R., Bass, L. A., Lewis, J. S., and McCarthy, D. W. (2001) Copper-64-TETA-octreotide as a PET Imaging Agent for Patients with Neuroendocrine Tumors. *J. Nucl. Med. 42*, 213−221.

(11) McCarthy, D. W., Shefer, R. E., Klinkowstein, R. E., Bass, L. A., Margenau, W. H., Cutler, C. S., Anderson, C. J., and Welch, M. J. (1997) The Efficient Production of High Specific Activity Cu-64 Using a Biomedical Cyclotron. *Nucl. Med. Biol. 24*, 35−43.

(12) McCarthy, D. W., Bass, L. A., Cutler, P. D., Shefer, R. E., Klinkowstein, R. E., Herrero, P., Lewis, J. S., Cutler, C. S., Anderson, C. J., and Welch, M. J. (1999) High Purity Production and Potential Applications of Copper-60 and Copper-61. *Nucl. Med. Biol. 26*, 351−358.

(13) Rosewicz, S., Vogt, D., Harth, N., Grund, C., Franke, W. W., Ruppert, S., Schweitzer, E., Riecken, E.-O., and Wiedenman, B. (1992) An Amphicrine Pancreatic Cell Line: AR42J Cells Combine Exocrine and Neuroendocrine Properties. *Eur. J. Cell Biol. 59*, 80−91.

(14) Christophe, J. (1994) Pancreatic Tumoral Cell Line AR42J: An Amphicrine Model. *Am. J. Physiol. (Gastrointest. Liver Physiol.) 266(29)*, G963-G971.

(15) Anderson, C. J., Pajeau, T. S., Edwards, W. B., Sherman, E. L. C., Rogers, B. E., and Welch, M. J. (1995) In vitro and in vivo Evaluation of Copper-64-Labeled Octreotide Conjugates. *J. Nucl. Med. 36*, 2315−2325.

(16) Lewis, J. S., Laforest, R., Lewis, M. R., and Anderson, C. J. (2000) Comparative Dosimetry of Copper-64 and Yttrium-90-labeled Somatostatin Analogues in a Tumor-bearing Rat Model. *Cancer Biother. Radiopharm. 15*, 593−604.

(17) Breeman, W. A. P., Hofland, L. J., Bakker, W. H., van der Pluijm, M., van Koetsveld, P. M., de Jong, M., Setyono-Han, B., Kwekkeboom, D. J., Visser, T. J., Lamberts, S. W. J., and Krenning, E. P. (1993) Radioiodinated Somatostatin Analogue RC-160: Preparation, Biological Activity, in vivo Application in Rats and Comparison with [^{123}I-Tyr³]octreotide. *Eur. J. Nucl. Med. 20*, 1089−1094.

(18) Foulon, C. F., Reist, C. J., Bigner, D. D., and Zalutsky, M. R. (2000) Radioiodination via D-amino Acid Peptide Enhances Cellular Retention and Tumor Xenograft Targeting of an Internalizing Anti-epidermal Growth Factor Receptor Variant III Monoclonal Antibody. *Cancer Res. 60*, 4453−4460.

(19) Lewis, J. S., Srinivasan, A., Schmidt, M. A., and Anderson, C. J. (1998) In vitro and in vivo Evaluation of ^{64}Cu-TETA-Tyr³-Octreotate. A New Somatostatin Analogues with Improved Target Tissue Uptake. *Nucl. Med. Biol. 26*, 267−273.

(20) Cherry, S. R., Shao, Y., Silverman, R. W., Meadors, K., Siegel, S., Chatziioannou, A., Young, J. W., Jones, W. F., Moyers, J. C., Newport, D., Boutenouchet, A., Farquhar, T. H., Andreaco, M., Paulus, M. J., Binkley, D. M., Nutt, R., and Phelps, M. E. (1997) MicroPET: a High-Resolution PET Scanner for Imaging Small Animals. *IEEE Trans. Nucl. Sci. 44*, 1161−1166.

(21) Bass, L. A., Wang, M., Welch, M. J., and Anderson, C. J. (2000) In vivo Transchelation of Copper-64 from TETA-octreotide to Superoxide Dismutase in Rat Liver. *Bioconjugate Chem. 11*, 527−532.

(22) Sun, X., Wuest, M., Weisman, G. R., Wong, E. H., Reed, D. P., Boswell, C. A., Motekaitis, R., Martell, A. E., Welch, M. J., and Anderson, C. J. (2002) Radiolabeling and in vivo Behavior of Copper-64-labeled Cross-Bridged Cyclam Ligands. *J. Med. Chem. 45*, 469−477.

(23) Lewis, J. S., Wang, M., Laforest, R., Wang, F., Erion, J. L., Bugaj, J. E., Srinivasan, A., and Anderson, C. J. (2001) Toxicity and Dosimetry of ^{177}Lu-DOTA-Y3-octreotate in a Rat Model. *Int. J. Cancer 94*, 873−877.

BC015590K

[CANCER RESEARCH 62, 445–449, January 15, 2002]

Copper-64-pyruvaldehyde-bis(N^4-methylthiosemicarbazone) for the Prevention of Tumor Growth at Wound Sites following Laparoscopic Surgery: Monitoring Therapy Response with microPET and Magnetic Resonance Imaging[1]

Jason S. Lewis, Judith M. Connett, Joel R. Garbow, Thomas L. Buettner, Yasuhisa Fujibayashi, James W. Fleshman, and Michael J. Welch[2]

Mallinckrodt Institute of Radiology [J. S. L., M. J. W.], and the Department of Surgery [J. M. C., T. L. B., J. W. F.], Washington University School of Medicine, St. Louis, Missouri 63110; The Department of Chemistry, Washington University, St. Louis, Missouri 63110 [J. R. G.]; and Biomedical Imaging Research Center, Fukui Medical University, Matsuoka, Fukui 910-1193, Japan [Y. F.]

ABSTRACT

Laparoscopic colectomy for curable colon cancer may result in the development of abdominal wall implants because of disseminated disease and the favorable environment of the wound site for cell implantation. Injection of disaggregated human GW39 colon cancer cells into the hamster peritoneum represents a model of tumor spillage that may occur during dissection, manipulation, resection, and extraction of tumor during surgery in the clinical setting. Using this well-established animal model, we tested the efficacy of ^{64}Cu-pyruvaldehyde-bis(N^4-methylthiosemicarbazone) (^{64}Cu-PTSM) in inhibiting tumor cell implantation in trocar wound sites. Anesthetized hamsters had four 5-mm trocars inserted through the anterior abdominal wall. GW39 cells (~3.2 × 10^4 cells in 0.5 ml) were injected into the peritoneum through a midline incision. Ten min later, hamsters were randomized to receive 5, 3, or 1 mCi of ^{64}Cu-PTSM through the same midline incision. High-resolution magnetic resonance imaging and microPET were used to monitor tumor volume and morphology after surgery. After 7 weeks, animals were sacrificed, and trocar and midline wounds were harvested for macroscopic and histological analysis. No macroscopic tumor was found in any of the group treated with 5 mCi of ^{64}Cu-PTSM, whereas 96% of the wound sites in the group treated with saline had macroscopic tumor growth ($P < 0.001$). This study demonstrates the therapeutic potential of ^{64}Cu-PTSM in inhibiting cancer cell implantation and growth at doses well below the maximum tolerated dose, with no signs of toxicity to the hamsters.

INTRODUCTION

Copper-64 [$t_{1/2}$ = 12.8 h; β^+ = 0.655 MeV (19%); β^- = 0.573 MeV (40%)] is a cyclotron-produced positron-emitting isotope (1, 2) that has utility in both diagnostic medicine (3, 4) and as a therapeutic radionuclide (5–8). The technology developed for the production of ^{64}Cu (Newton Scientific, Inc., Cambridge, MA) has been obtained by institutions in the United States, Europe, Japan, and Canada. ^{64}Cu-PTSM[3] belongs to a class of neutral, lipophilic complexes that have demonstrated rapid diffusion into cells. In experiments using cultured single-cell suspensions of EMT6 mammary carcinoma cells, 80% of ^{64}Cu-PTSM added was retained within the cells after only 1 min (9). Recently we showed that the hypoxia-selective ^{64}Cu-ATSM, an analogue of Cu-PTSM, has promise as an agent for radiotherapy by significantly increasing the survival time of hamsters bearing solid tumors without acute toxicity (8).

Laparoscopic colectomy is the process of resecting portions of the colon, using trocars, video laparoscopy, and carbon dioxide pneumoperitoneum to minimize abdominal wall access. The use of laparoscopic colectomy for curable colon cancer remains controversial because of the documentation of metastasis at the incision sites (10, 11). Since 1993, there have been a number of case reports of tumor recurrence at trocar sites following laparoscopic colon resections (12, 13). The development of abdominal wall implants may be attributable to bonafide disseminated disease or to tumor cells disseminated by surgical manipulation and the favorable environment of the wound site for cell implantation. At Washington University Medical School, a hamster model of colorectal cancer has been developed that mimics the implantation of cancer cells following invasive surgery (14, 15). In this model, injection of disaggregated human GW39 colon cancer cells into the hamster peritoneum represents a model of tumor spillage that may occur during dissection, manipulation, resection, and extraction of tumor during an operation.

The present work is based on the hypothesis that therapeutic doses of ^{64}Cu-PTSM could ablate any loose tumor cells within the abdomen. This idea is based on the evidence obtained *in vitro* that uptake of Cu-PTSM in single-cell suspensions is rapid and quantitative as described above. The present investigation was performed to test this hypothesis by measuring the ability of ^{64}Cu-PTSM to inhibit the implantation of loose cancer cells in wound sites following laparoscopic surgery.

MATERIALS AND METHODS

Materials. ^{64}Cu was produced on a CS-15 biomedical cyclotron at Washington University School of Medicine, using published methods (2). ^{64}Cu-PTSM was synthesized as described previously (9, 16). Unless otherwise stated, all chemicals were purchased from Aldrich Chemical Company, Inc. (Milwaukee, WI). All solutions were prepared with distilled deionized water (Milli-Q; >18 megaohm resistivity). Radiochemical purity of ^{64}Cu-PTSM in all studies was >98% as determined by radio-TLC.

Animal Models. All animal experiments were conducted in compliance with the Guidelines for the Care and Use of Research Animals established by Washington University's Animal Studies Committee. Biodistribution data in nontumor-bearing hamsters were obtained by administering ^{64}Cu-PTSM (10 μCi) i.p. to 100-g golden Syrian hamsters (Sasco Inc., Omaha, NE). The hamsters (n = 5 each group) were euthanized at 5, 30, 120, and 240 min postinjection. Selected tissues and organs were harvested, and weighed, and the activity was counted on a gamma counter. The percentage of injected dose per gram and percentage of injected dose per organ for each tissue were calculated. The laparoscopic model was performed according to previously reported methods (14, 15). Briefly, anesthetized golden Syrian hamsters (100 g) had four 5-mm trocars inserted through the anterior abdominal wall; GW39 cells (~3.2 × 10^4 cells in 0.5 ml of PBS) were then injected into the peritoneum through a 2-cm midline incision. Trocars were then removed, and the trocar wounds were closed. Viability of cells was confirmed to be 98% at the time of injection with Trypan vital blue staining.

Received 7/17/01; accepted 11/5/01.

The costs of publication of this article were defrayed in part by the payment of page charges. This article must therefore be hereby marked *advertisement* in accordance with 18 U.S.C. Section 1734 solely to indicate this fact.

[1] This work was supported by a grant from the United States Department of Energy (Grant DE-FG02-87ER60512). The production of copper radionuclides at Washington University is supported by a grant from the National Cancer Institute (Grant 1 R24 CA86307), and the small animal imaging at Washington University is supported by United States NIH Grant 5 R24 CA83060.

[2] To whom requests for reprints should be addressed, at Mallinckrodt Institute of Radiology, Washington University School of Medicine, 510 S. Kingshighway Boulevard, Campus Box 8225, Saint Louis, MO 63110. Phone: (314) 362-8435; Fax: (314) 362-8399; E-mail: welchm@mir.wustl.edu.

[3] The abbreviations used are: ^{64}Cu-PTSM, ^{64}Cu-pyruvaldehyde-bis(N^4-methylthiosemicarbazone); ^{64}Cu-ATSM, ^{64}Cu-diacetyl-bis(N^4-methylthiosemicarbazone); MRI, magnetic resonance imaging; ^{18}F-FDG, [^{18}F]fluoro-2-deoxyglucose; MAb, monoclonal antibody; PET, positron emission tomography; MTD, maximum tolerated dose.

Radiotherapy Experiments. Following laparoscopic surgery as described above, hamsters ($n \geq 7$ in each group) were randomized to receive saline or 1, 3, or 5 mCi of ^{64}Cu-PTSM. Radioactivity was given within 10 min of surgery through the sutured midline incision. The hamsters were provided water and hamster chow immediately after the operation and inspected daily for evidence of complications. Seven weeks after surgery and radiotherapy, animals were sacrificed, and trocar and midline wounds were examined for macroscopic tumor. Wound sites without gross tumor were excised, fresh frozen, and examined histologically for the presence of microscopic tumor implants. The tumors were examined histologically *ex vivo*, using H&E and Mucin staining techniques (15). The Diagnostic Services Laboratory in the Department of Comparative Medicine at Washington University School of Medicine performed toxicity analysis on select animals from the 5 mCi-treated animals. The hematology analysis included hemoglobin, WBC counts, RBC counts, platelet counts, hematocrit, and differential WBCs. Liver and kidney analyses included blood urea nitrogen, creatinine, alanine aminotransferase, and aspartate aminotransferase.

Imaging. High resolution MRI and microPET (Concorde Microsystems; Knoxville, TN) were used to monitor tumor volume and morphology after surgery. Hamsters were imaged weekly in an Oxford Instruments 200/330 (4.7 tesla; 33-cm clear bore) magnet equipped with a 16 cm (i.d.) actively shielded gradient coil (maximum gradient, 18 G/cm; rise time; 400 μs). The magnet and gradient coil were interfaced to a Varian UNITY-*INOVA* console. Magnetic resonance images were collected weekly following laparoscopic surgery, and tumor growth was measured by manually segmenting individual slices in each image and calculating volumes using Varian's Image Browser software. To confirm the presence of established GW39 tumors in control animals, 2 weeks after the initial surgery, select animals were injected with tracer amounts of ^{64}Cu-PTSM (200–250 μCi) and imaged on the microPET 2-h postinjection. One week later, these same select hamsters were injected with tracer amounts of ^{64}Cu-TETA-1A3 (Refs. 3, 7; 200–250 μCi) and imaged 2-h postinjection. An additional group of control hamsters was also imaged with ^{18}F-FDG on the microPET at 3, 5, and 7 weeks post surgery. In each imaging session, fasted hamsters received injections containing ~1 mCi of ^{18}F-FDG and were imaged at 1 h postinjection. A third group of hamsters that underwent the same laparoscopic operation (trocar and midline incision), but did not receive GW39 cells, underwent both ^{18}F-FDG-microPET and ^{64}Cu-PTSM-microPET as controls. Tumor volume from the microPET images was determined using AnalyzeAVW 3.0 (Biomedical Imaging Resource, Rochester, MN).

Statistical Analysis. To determine statistical significance, a Student's t test was performed and a 95% confidence level assumed, with $P < 0.05$ being considered significantly different. χ^2 or Fisher's exact tests were used to compare proportions and frequency data.

RESULTS

Biodistribution Studies. The data obtained from the biodistribution of ^{64}Cu-PTSM in nontumor-bearing hamsters are shown in Table 1. ^{64}Cu-PTSM exits the peritoneum to enter the blood stream within 5 min to reach a maximum blood level at 120 min postinjection. ^{64}Cu-PTSM is then seen to distribute to all of the organs harvested, including the heart, brain, and lung, again reaching maximum uptake values at 120 min postinjection. ^{64}Cu-PTSM is cleared through the liver and kidney. Liver uptake is followed by uptake in the intestines prior to excretion. The uptake observed in the intestines, however, could also be attributed to uptake by the intact serosa of the bowel and intact peritoneum directly following the i.p. injection of radioactivity and not from the normal excretory pathways. It is important to note that the systemic administration of ^{64}Cu-PTSM results in a much more rapid distribution of the tracer, with peak values being reached more rapidly and larger amounts of radioactivity being taken up by the organs examined (8, 9).

Table 1 *Biodistribution (percentage of injected dose/g ± SD, n = 4) at 5, 30, 120, and 240 min of ^{64}Cu-PTSM in nontumor-bearing hamsters*

Organ	5 min	30 min	120 min	240 min
Blood	0.43 ± 0.22	0.77 ± 0.06	0.81 ± 0.26	0.54 ± 0.06
Brain	0.26 ± 0.08	0.25 ± 0.04	0.85 ± 0.32	0.32 ± 0.04
Heart	0.92 ± 0.24	0.77 ± 0.11	1.83 ± 0.57	1.31 ± 0.39
Lung	0.88 ± 0.28	0.72 ± 0.09	1.91 ± 0.71	1.04 ± 0.35
Muscle	0.26 ± 0.10	1.47 ± 0.83	0.94 ± 0.16	0.66 ± 0.18
Liver	0.24 ± 0.08	2.74 ± 0.32	5.56 ± 1.37	4.04 ± 0.40
Kidney	0.92 ± 0.30	2.69 ± 0.41	3.65 ± 0.92	2.16 ± 0.15
Stomach	0.13 ± 0.04	1.29 ± 0.86	2.50 ± 3.20	0.95 ± 0.15
Sm int[a]	0.42 ± 0.32	2.56 ± 0.85	3.06 ± 0.71	1.77 ± 0.14
Cecum	0.47 ± 0.31	2.74 ± 1.07	3.52 ± 1.58	3.12 ± 0.34
Lg int	0.27 ± 0.10	1.70 ± 1.35	1.45 ± 1.00	2.17 ± 0.52

[a] Sm int, small intestine; Lg int, large intestine.

Table 2 *GW39 tumor implantation following therapy with 1, 3, or 5 mCi of ^{64}Cu-PTSM*

	1 mCi	3 mCi	5 mCi	Control
No. of hamsters	10	7	9	10
Total positive sites (n)	37	8	1	35
Total negative sites (n)	8	27	44	0
% Positive	82	23	2	100
Macro evaluation				
Total positive sites (n)	24	4	0	35
Total negative sites (n)	21	31	45	0
Tumor volume (g)	0.28 ± 0.22	0.14 ± 0.06	0.00 ± 0.00	14.48 ± 3.98
% Positive	53	11	0	100
Micro evaluation				
Total positive sites (n)	13	4	1	
Total negative sites (n)	8	27	44	
% Positive	62	13	2	

Radiotherapy Experiments. There were no premature deaths in any of the experimental or control groups, and growth of tumors occurred only at the port and midline incision sites. The results clearly demonstrated the ability of ^{64}Cu-PTSM to inhibit the implantation of tumors in wound sites in a dose-dependent manner (Table 2). After treatment with 1 mCi of ^{64}Cu-PTSM, 17.8% inhibition of tumor implantation inhibition was noted, compared with 66.8% inhibition when 3 mCi was administered. In hamsters treated with 5 mCi of ^{64}Cu-PTSM, there was no evidence of macroscopic tumor in any of the animals. Conversely, in the saline control animals ($n = 10$), all of the wound sites ($n = 35$) had macroscopic tumor growth ($P < 0.001$). When examined microscopically, the animals treated with 5 mCi exhibited only 2% tumor implantation in the total possible wound sites. The doses administered to achieve inhibition did not produce any signs of toxicity in the animals: the mean weight of the treated hamsters increased similarly to that of the control hamsters, and they maintained a healthy physical appearance (with no sign of scruffy coat or diarrhea) over the experimental period. There were no significant changes in blood chemistry levels. Animals receiving H_2-PTSM or nonradioactive Cu-PTSM in amounts equivalent to those in the radioactive studies had survival rate identical to that of the vehicle controls (data not shown).

Imaging. Magnetic resonance images of hamster abdominal cavities clearly showed tumor development and growth. The presence of tumors in the GW39-treated animals was clearly seen in these images. The uptake of ^{64}Cu-PTSM and ^{64}Cu-TETA-1A3 in the abdomen of hamsters as monitored by microPET is shown in Fig. 1*A*. The images demonstrate that the regional uptake of both agents in the hamster's abdomen are in very good agreement, despite the different specificities of the agents. The size, number, and location of tumors visualized in these microPET studies matched well with subsequent histological analysis performed 7 weeks postsurgery (*i.e.*, in each animal imaged, the regional uptake of the ^{64}Cu-labeled agents as visualized by microPET corresponded to abnormal mass observed by MRI, which was subsequently confirmed by histology to be GW39 tumor). The uptake of ^{18}F-FDG in the abdomen of hamsters as monitored by microPET was localized in tumors (Fig. 1*B*) as demonstrated by examining the magnetic resonance images and, subsequently, the animals at

Table 3 *Tumor volume (g) determined by microPET, MRI, and subsequent histology*
The values obtained by MRI reflect the more accurate determination of tumor volume obtained by imaging techniques.

Hamster	microPET	MRI	Histology
1	0.12	0.15	0.167
2	0.08	0.07	0.074
3	4.21	4.98	4.95
4	0.54	0.55	0.562

strated by ^{64}Cu-PTSM in cultured cell suspensions (9) make this an ideal candidate for the studies described herein. In the present study, ^{64}Cu-PTSM was investigated as a potential radiotherapy agent for the ablation of loose cells created by surgical manipulation or in disseminated disease. Because of the nonspecific uptake mechanisms of the agent, it is reasonable to assume that ^{64}Cu-PTSM would not only discriminate between injected viable cells but also between separated tumor cells, viable cells such as i.p. macrophages, or cells that have been liberated from a primary tumor.

The biodistribution data presented in this report demonstrate that although ^{64}Cu-PTSM does exit from the intact peritoneum, it does so at a much slower rate than that following systemic administration of the agent (9). The levels of radioactivity in the tissues examined after administration of ^{64}Cu-PTSM are relatively low, suggesting retention of the radioactivity in the peritoneum, which allows easy accessibility of the agent to the loose tumor cells introduced earlier into the cavity in this animal model.

The therapy results clearly demonstrated the ability of ^{64}Cu-PTSM to inhibit the implantation and formation of tumors. The delivery of the radiotherapy agent was performed 10 min after the inoculation of cells, a time point that may not be clinically realistic; thus, additional studies may be required to determine the most efficient time of administration postsurgery. Following the administration of 5 mCi of ^{64}Cu-PTSM, there was no macroscopic evidence of tumor at any wound site after 7 weeks. Furthermore, only 2% of the possible sites showed the presence of microscopic tumors. This inhibition was achieved in a dose-dependent manner that did not produce overt signs of toxicity in the animals. Therefore, the toxicity data indicate that the MTD for this compound was not achieved and that larger quantities of radioactivity could be administered safely. In the ^{64}Cu-ATSM study with solid GW39 tumors, animals that received 10 mCi of ^{64}Cu-ATSM i.v. displayed a transient depression in WBC counts, platelets, and liver enzyme levels, but no significant changes in the total protein, hemoglobin, RBC, and kidney enzyme levels (8). It is therefore not surprising that the administration of 5 mCi of ^{64}Cu-PTSM i.p. produced significantly lower toxicity than the systemic administration of 10 mCi of ^{64}Cu-ATSM. Previous studies showed that targeted radiotherapy with ^{131}I-labeled MAb 1A3 (1 mCi) was well tolerated in the hamster and showed a 47% inhibition of tumor growth in the GW39 laparoscopic model.[4] ^{64}Cu compares well with the ^{131}I data: 5 mCi of the nonspecific ^{64}Cu-PTSM produced 98% inhibition of tumor growth. Prior to human use, we will determine the MTD of ^{64}Cu-PTSM in an animal model in which peritoneal or retroperitoneal dissection procedures may yield a more realistic MTD value.

The efficient therapeutic kill noted in this study can best be explained by the fact that in subcellular fractionation studies, a significant portion of the ^{64}Cu-PTSM was delivered to the cell nucleus following uptake (>20% after 24 h; Refs. 25, 26). ^{64}Cu emits a 0.58-MeV β^- particle (40%), a 0.66-MeV β^+ particle (19%), and a γ of 1.34 MeV (0.5%), giving a mean range of penetrating radiation of <1 mm in tissue. During decay by electron capture, the copper radionuclide emits highly radiotoxic Auger electrons with high linear energy transfer that have a tissue penetration of 0.02–10 μm, the approximate cell nucleus diameter. Therefore, the Auger electrons would be very toxic if the DNA of the cell is within range (27). Because of their short range and relatively larger linear energy transfer, low-energy Auger electrons potentially are more radiotoxic than the higher energy positron or β^- particles. Additionally, ^{64}Cu has a maximum recoil energy resulting from the nuclear transmutation of the copper ion (from β^- = 7.6 eV; from β^+ = 9.15 eV; Ref. 28) to its highly charged daughter nucleus, which may also increase the cell-killing ability. Copper ions have also been implicated in the maintenance of the nuclear matrix and in DNA folding (29). It is also known that the treatment of isolated nuclei with low levels of Cu(II) causes nuclear matrix-associated DNA binding and DNA-protein cross-linking as well as DNA double-strand breaks following irradiation (30). The combination of these characteristics may help explain ^{64}Cu toxicity. It is important to note that because low-energy Auger electrons deposit their energy in a very small volume and the ^{64}Cu is likely very close to DNA, conventional macroscopic dose calculations would most likely underestimate the energy imparted and thus the absorbed dose. A microdosimetric approach to future tumor/tumor cell dose calculations that accounts for all Auger electrons could raise estimates and relate more closely to the observed tumor cell kill.

The uptake of ^{64}Cu-PTSM and ^{64}Cu-TETA-MAb-1A3 in the abdomens of hamsters as monitored by microPET was latter confirmed by histology to localize in established GW39 tumors. This is of particular importance when attempting to monitor the biokinetics of the ^{64}Cu agents and for calculating the absorbed doses delivered by a therapeutic dose of ^{64}Cu-labeled radiopharmaceuticals, as were previously shown possible in studies with solid GW39 tumor (8). It is, however, important to note that the biokinetics of ^{64}Cu-PTSM are dependent on blood flow. Despite the fact the edges of the tumors are likely to be well vascularized, areas of decreased blood perfusion in a metastasis would have decreased tracer retention, perhaps leading to inaccurate estimation of tumor volume with microPET. Moreover, for imaging purposes in this particular study, the use of ^{64}Cu agents to monitor tumor growth and response may not be appropriate: repeated administration of small amounts of ^{64}Cu for microPET imaging may lead to tumor regression, leading to an inaccurate assessment of therapeutic efficacy of the drug under investigation. Therefore, in this study, the use of the nontherapeutic ^{18}F-FDG was explored to monitor the biochemical responses of the tumors to treatment. Historically, the assessment of tumor geometry and volume has been by the use of caliper measurements. Not only is this mode of measurement limited by the tumor's irregular shape, it does not yield any physiological information during radiotherapy experiments. In the present study, MRI showed the presence GW39 tumors in trocar sites in the abdomen of animals and allowed for more accurate determination of tumor volume compared with the microPET results (Table 3). The use of microPET for volume determination, although accurate for small tumor masses, displayed large discrepancies with larger tumor volumes, presumably as a result of extensive tumor necrosis not visualized by ^{18}F-FDG-microPET (Table 3). The use of MRI for volume determination allows for the inclusion of all tumor tissue, including necrotic, that may not otherwise be visualized with the radiopharmaceuticals used in this study.

MRI and microPET experiments using ^{18}F-FDG, demonstrated that the abdominal tumor could be easily detected and that growth could be monitored (Fig. 1*B*). Furthermore, ^{18}F-FDG imaging confirmed the growth of tumors at the sites of trocar placement and midline incision (Fig. 1*C*). The use of histology further confirmed the presence of tumors, but most importantly identified the presence of microscopic tumors that could not be delineated with the imaging techniques.

[4] J. M. Connett *et al.*, Radioimmunotherapy of colon cancer in a laparoscopic model using I-131-MAb-1A3, manuscript in preparation.

MicroPET images in conjunction with MRI imaging yielded information and data not normally available with the use of caliper measurements. These results indicate that microPET and MRI can help determine overall treatment effectiveness and monitor therapeutic response and, as such, form a powerful combination of imaging modalities that will find broad application in the characterization of disease states and the development of therapeutics.

Radiotherapeutic effectiveness depends on radioligand delivery to and subsequent accumulation within the cell. Unlike many other radiopharmaceuticals that rely on the high accessibility and up-regulation of antigens, ^{64}Cu-PTSM is a nonreceptor-based agent. Therapeutic quantities of ^{64}Cu-PTSM inhibited GW39 implantation in wound sites with no acute toxicity. In the laparoscopic study, the administration of ^{64}Cu-PTSM into the abdomen produced rapid uptake and ablation of loose tumor cells, resulting in significant reduction of tumor implantation at wound sites. Additional work is required to study the effects of different levels of tumor burden, timing effects, and the quantification of normal tissue dosimetry. This was a proof-of-principle study to examine the use of ^{64}Cu-PTSM treatment as an adjuvant therapy for the inhibition of tumor cell implantation following surgery and not for the treatment of existing primary tumors. Future work will include investigating whether the rapid uptake kinetics of ^{64}Cu-PTSM could also allow this agent to be used for the treatment of accessible tumors by direct intratumoral delivery or for treatment of cancer in the peritoneum, *e.g.,* ovarian tumors, ascites, or carcinomatoses in colorectal cancer (*e.g.,* as a means of reducing local and pelvic recurrences).

In conclusion, addition of ^{64}Cu to the radiotherapy arsenal is both useful and innovative because it allows accurate monitoring of drug distribution and biokinetics through concurrent PET imaging. This study has demonstrated the therapeutic potential of ^{64}Cu-PTSM in inhibiting cancer cell attachment to incision sites and growth of metastasis following laparoscopy surgery. ^{64}Cu-PTSM was shown to inhibit cancer cell implantation and growth at a dose that resulted in no overt signs of toxicity to the hamsters. We have also shown that MRI and PET provided powerful imaging modalities for monitoring tumor growth and development following therapy.

ACKNOWLEDGMENTS

We thank Dr. Deborah W. McCarthy and Todd A. Perkins for production of ^{64}Cu, and Drs. Dan Ye, Richard Laforest, Douglas J. Rowland, Joon Young Kim, and Wenping Li for assistance. We also thank Suzanne Hickerson, Terry Sharp, and John Engelbach for excellent technical support.

REFERENCES

1. Blower, P. J., Lewis, J. S., and Zweit, J. Copper radionuclides and radiopharmaceuticals in nuclear medicine. Nucl. Med. Biol., *23:* 957–980, 1996.
2. McCarthy, D. W., Shefer, R. E., Klinkowstein, R. E., Bass, L. A., Margeneau, W. H., Cutler, C. S., Anderson, C. J., and Welch, M. J. Efficient production of high specific activity ^{64}Cu using a biomedical cyclotron. Nucl. Med. Biol., *24:* 35–43, 1997.
3. Philpott, G. W., Schwarz, S. W., Anderson, C. J., Dehdashti, F., Connett, J. M., Zinn, K. R., Meares, C. F., Cutler, P. D., Welch, M. J., and Siegel, B. A. RadioimmunoPET: detection of colorectal carcinoma with positron-emitting copper-64-labeled monoclonal antibody. J. Nucl. Med., *36:* 1818–1824, 1995.
4. Cutler, P. D., Schwarz, S. W., Anderson, C. J., Connett, C. J., Welch, M. J., Philpott, G. W., and Siegel, B. A. Dosimetry of copper-64-labeled monoclonal antibody 1A3 as determined by PET imaging of the torso. J. Nucl. Med., *36:* 2363–2371, 1995.
5. Lewis, J. S., Lewis, M. R., Cutler, P. D., Srinivasan, A., Schmidt, M. A., Schwarz, S. W., Morris, M. M., Miller, J. P., and Anderson, C. J. Radiotherapy and dosimetry of ^{64}Cu-TETA-Tyr^3-octreotate in a somatostatin receptor-positive, tumor bearing rat model. Clin. Cancer Res., *5:* 3608–3616, 1999.
6. Anderson, C. J., Jones, L. A., Bass, L. A., Sherman, E. L. C., McCarthy, D. W., Cutler, P. D., Lanahan, M. V., Cristel, M. E., Lewis, J. S., and Schwarz, S. W. Radiotherapy, toxicity and dosimetry of copper-64-TETA-octreotide in tumor bearing rats. J. Nucl. Med., *39:* 1944–1951, 1998.
7. Connett, J. M., Buettner, T. L., and Anderson, C. J. Maximum tolerated dose and large tumor radioimmunotherapy studies of ^{64}Cu-labeled monoclonal antibody 1A3 in a colon cancer model. Clin. Cancer Res., *5:* 3207s–3212s, 1999.
8. Lewis, J. S., Laforest, R., Buettner, T. L., Song, S-K., Fujibayashi, Y., Connett, J. M., and Welch, M. J. Copper-64-diacetyl-bis(N^4-methylthiosemicarbazone): an agent for radiotherapy. Proc. Natl. Acad. Sci. USA, *98:* 1206–1211, 2001.
9. Lewis, J. S., McCarthy, D. W., McCarthy, T. J., Fujibayashi, Y., and Welch, M. J. The evaluation of. 64Cu-diacetyl-bis(N^4-methylthiosemicarbazone) (^{64}Cu-ATSM) *in vivo* and *in vitro* in a hypoxic tumor model: J. Nucl. Med., *40:* 177–183, 1999.
10. Ota, D. M. Laparoscopy colectomy for cancer: a favorable opinion. Ann. Surg. Oncol., *2:* 3–5, 1995.
11. Berman, I. R. Laparoscopic colectomy for cancer: some cause for pause. Ann. Surg. Oncol., *2:* 1–2, 1995.
12. Wexner, S. D., and Cohen, S. M. Port site metastasis after laparoscopic colorectal surgery for cure of malignancy. Br. J. Surg., *82:* 295–298, 1995.
13. Alexander, R. J., Jacques, B. C., and Mitchell, K. G. Laparoscopically assisted colectomy and wound recurrence. Lancet., *341:* 249–250, 1993.
14. Jones, D. B., Guo, L-W., Reinhard, M. K., Soper, N. J., Philpott, G. W., Connett, J., and Fleshman, J. W. Impact of pneumoperitoneum on trocar site implantation of colon cancer in hamster model. Dis. Colon Rectum., *38:* 1182–1188, 1995.
15. Wu, J. S., Brasfield, E. B., Guo, L-W., Ruiz, M., Connett, J. M., Philpott, G. W., Jones, D. B., and Fleshman, J. W. Implantation of colon cancer at trocar sites is increased by low pressure pneumoperitoneum. Surgery., *122:* 1–8, 1997.
16. Fujibayashi, Y., Cutler, C. S., Anderson, C. J., McCarthy, D. W., Jones, L. A., Sharp, T., Yonekura, Y., and Welch, M. J. Comparative imaging studies of ^{64}Cu-ATSM a hypoxia imaging agent and C-11-acetate in an acute myocardial infarction model: *ex vivo* imaging in rats. Nucl. Med. Biol., *26:* 117–121, 1999.
17. Connett, J. M., Anderson, C. J., Guo, L. W., Schwarz, S. W., Zinn, K. R., Rogers, B. E., Siegel, B. A., Philpott, G. W., and Welch, M. J. Radioimmunotherapy with a Cu-64-labeled monoclonal antibody: a comparison with Cu-67. Proc. Natl. Acad. Sci. USA, *93:* 6814–6818, 1996.
18. Lewis, J. S., Sharp, T. L., Laforest, R., Fujibayashi, Y., and Welch, M. J. Tumor uptake of copper-diacetyl-bis(N^4-methylthiosemicarbazone): effect of changes in tissue oxygenation. J. Nucl. Med., *42:* 655–661, 2001.
19. Dearling, J. L. D., Lewis, J. S., Mullen, G. E. D., Rae, M. T., Zweit, J., and Blower, P. J. Design of hypoxia-targeting radiopharmaceuticals: selective uptake of copper-64 complexes in hypoxic cells in vitro. Eur. J. Nucl. Med., *25:* 788–792, 1998.
20. Dearling, J. L. J., Lewis, J. S., Welch, M. J., McCarthy, D. W., and Blower, P. J. Redox-active complexes for imaging hypoxic tissues: structure-activity relationships in copper(II) bis(thiosemicarbazone) complexes. Chem. Commun., *22:* 2531–2533, 1998.
21. Fujibayashi, Y., Wada, K., Taniuchi, H., Yonekura, Y., Konishi, J., and Yokoyama, A. Mitochondria-selective reduction of ^{62}Cu-pyruvaldehyde-bis(N^4-methylthiosemicarbazone) (^{62}Cu-PTSM) in the murine brain; a novel radiopharmaceutical for brain positron emission tomography (PET) imaging. Biol. Pharm. Bull., *16:* 146–149, 1993.
22. Fujibayashi, Y., Taniuchi, H., Yonekura, Y., Ohtani, H., Konishi, J., and Yokoyama, A. Copper-62-ATSM: a new hypoxia imaging agent with high membrane permeability and low redox potential. J. Nucl. Med., *38:* 1155–1160, 1997.
23. Green, M. A., Mathias, C. J., Welch, M. J., McGuire, A. H., Perry, D., Fernandez-Rubio, F., Perlmutter, J. S., Raichle, M. E., and Bergmann, S. R. Copper-62-labeled pyruvaldehyde bis(N^4-methylthiosemicarbazonato)-copper(II): synthesis and evaluation as a positron emission tomography tracer for cerebral and myocardial perfusion. J. Nucl. Med., *31:* 1989–1996, 1990.
24. Taniuchi, H., Fujibayashi, Y., Yonekura, Y., Konishi, J., and Yokoyama, A. Hyperfixation of copper-62-PTSM in rat brain after transient global ischemia. J. Nucl. Med., *38:* 1130–1134, 1997.
25. Baerga, I. D., Maickel, R. P., and Green, M. A. Subcellular distribution of tissue radiocopper following intravenous administration of ^{67}Cu-labeled Cu-PTSM, Nucl. Med. Biol., *19:* 697–701, 1992.
26. Shibuya, K., Fujibayashi, Y., Yoshimi, E., Sasai, K., Hiraoka, K., and Welch, M. J. Cytosolic/microsomal redox pathway: a reductive retention mechanism of a PET-oncology tracer, Cu-pyruvaldehyde-bis(N^4-methylthiosemicarbazone) (Cu-PTSM). Ann. Nucl. Med., *13:* 287–292, 1999.
27. Adelstein, S. J. The Auger process: a therapeutic promise?. Am. J. Roentgenol., *160:* 707–713, 1993.
28. Wahl, A. C., and Bonner, N. A. Radioactivity Applied to Chemistry, pp. 511–514. New York: John Wiley & Sons, 1951.
29. George, A. M., Sabovljev, S. A., Hart, L. E., Cramp, W. A., Harris, G., and Hornsey, S. DNA quaternary structure in the radiation sensitivity of human lymphocytes—a proposed role of copper. Br. J. Cancer, *55* (Suppl. VIII): 141–144, 1987.
30. Chiu, S-M., Xue, L-Y., Friedman, L. R., and Oleinick, N. L. Copper ion-mediated sensitization of nuclear matrix attachment sites to ionizing radiation. Biochemistry., *32:* 6214–6219, 1993.

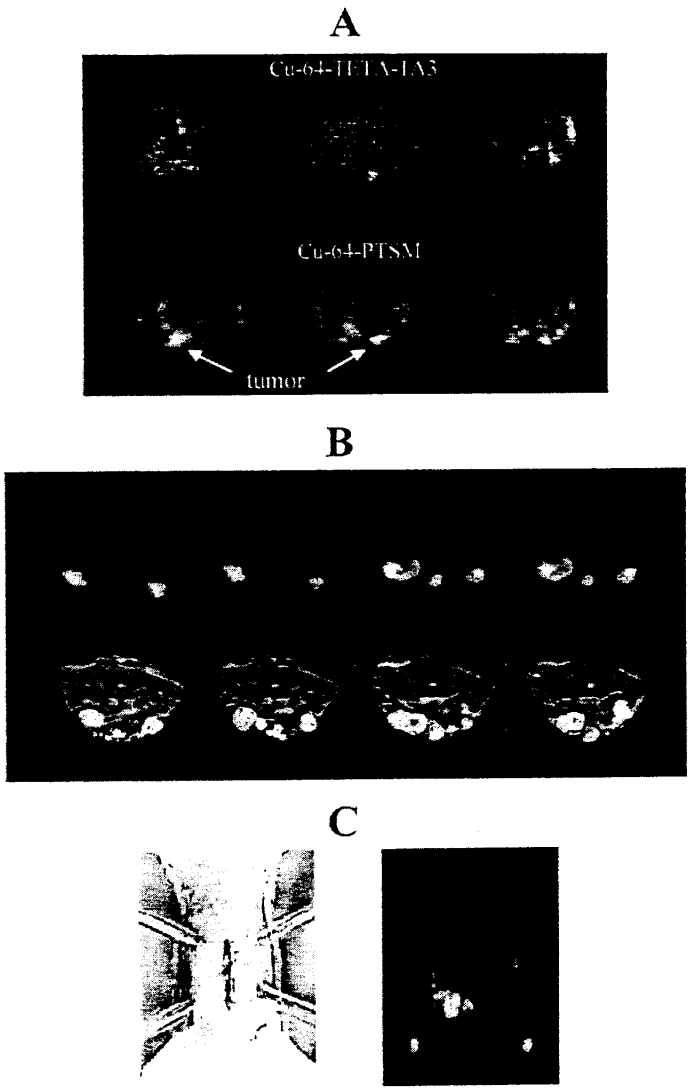

Fig. 1. *A*, transaxial microPET images (where the anterior surface of the animal is at the *bottom* of the image) of a GW39-treated hamster 2 (^{64}Cu-PTSM) and 3 (^{64}Cu-TETA-1A3) weeks after laparoscopic surgery. Tumors are seen as *bright spots* in these images. *B*, transaxial microPET and MRI images (where the anterior surface of the animal is at the *bottom* of the image) of a hamster 6 weeks after laparoscopic surgery. The *bright spots* in the PET images (*top*) indicate areas of increased ^{18}F accumulation, which coincide in position with abdominal tumors that can be clearly visualized in the MRI images (*bottom*). *C*, photograph of a hamster abdomen showing the sites of trocar placement and midline incision (*left*) and coronal microPET image of a hamster 6 weeks after laparoscopic surgery (*right*). The *bright spots* in the PET image (*right*) indicate areas of increased ^{18}F accumulation, which coincide in position with abdominal tumors, which further correspond to the trocar and midline incision sites (*left*). In control animals that did not receive any GW39 cells, no apparent uptake was observed at the incision sites (data not shown).

the time of sacrifice (Table 3). On examination of the ^{18}F-FDG coronal images, the visualized tumors were located at the points of trocar placement and midline incision, confirming the growth of tumor at the points of surgical manipulation (Fig. 1*C*). In the control animals that underwent surgery but were not given GW39 cells, no detectable activity had accumulated in the incision sites with ^{18}F-FDG-microPET or ^{64}Cu-PTSM-microPET at the same imaging time points.

DISCUSSION

^{64}Cu is a cyclotron-produced isotope that has applications both in PET and radiotherapy. The addition of ^{64}Cu to the radiotherapy arsenal is particularly innovative because it enables the accurate monitoring of biodistribution and biokinetics through concurrent PET imaging. To date, ^{64}Cu-radiotherapy studies have included the use of the ^{64}Cu-labeled MAb 1A3 (17) and ^{64}Cu-labeled somatostatin-based peptides (5, 6). Recently, we showed that the hypoxia-selective ^{64}Cu-ATSM inhibits the growth of GW39 tumors in hamsters with no acute toxicity (8).

Cu-PTSM belongs to a group of compounds that can be classed as either nonhypoxia-selective (*e.g.*, Cu-PTSM) or hypoxia selective (*e.g.*, Cu-ATSM; Refs. 9, 18–24). ^{62}Cu-PTSM has been evaluated clinically as a radiopharmaceutical for myocardial and cerebral perfusion imaging with PET (23). The rapid uptake and kinetics demon-